# Brine utilisation for cooling and salt production in wind-driven seawater greenhouses: Design and modelling
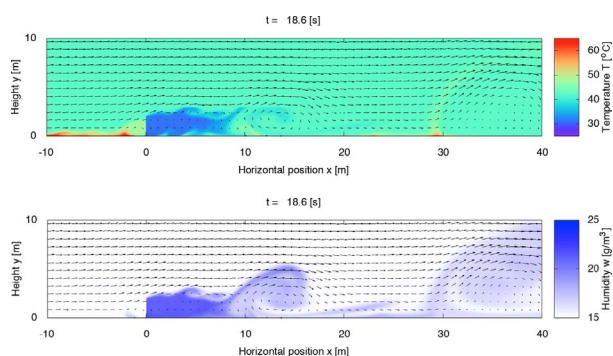
T. Akinaga[a], S.C. Generalis[a], C. Paton[b], O.N. Igobo[a], P.A. Davies[a,*]

[a] School of Engineering and Applied Science, Aston University, Birmingham B4 7ET, UK
[b] Seawater Greenhouse Ltd, London E8 1AB, UK

## GRAPHICAL ABSTRACT



## ARTICLE INFO

## ABSTRACT

Brine disposal is a major challenge facing the desalination industry. Discharged brines pollute the oceans and aquifers. Here is it proposed to reduce the volume of brines by means of evaporative coolers in seawater greenhouses, thus enabling the cultivation of high-value crops and production of sea salt. Unlike in typical greenhouses, only natural wind is used for ventilation, without electric fans. We present a model to predict the water evaporation, salt production, internal temperature and humidity according to ambient conditions. Predictions are presented for three case studies: (a) the Horn of Africa (Berbera) where a seawater desalination plant will be coupled to salt production; (b) Iran (Ahwaz) for management of hypersaline water from the Gotvand dam; (c) Gujarat (Ahmedabad) where natural seawater is fed to the cooling process, enhancing salt production in solar salt works. Water evaporation per face area of evaporator pad is predicted in the range 33 to 83 $m^3/m^2 \cdot yr$, and salt production up to 5.8 tonnes/$m^2 \cdot yr$. Temperature is lowest close to the evaporator pad, increasing downwind, such that the cooling effect mostly dissipates within 15 m of the cooling pad. Depending on location, peak temperatures reduce by 8–16 °C at the hottest time of year.

## 1. Introduction

Disposal of brines from desalination plants is considered one of the major challenges associated with the desalination industry today. Many studies have been presented concerning brine management options, mineral recovery, and 'Zero liquid discharge' (ZLD) [1–3]. Nonetheless, improved brine disposal is still quite rare in practice. Indeed almost all brine from seawater desalination plants is disposed of directly to the oceans. The quantity of brine is comparable to that of freshwater produced by desalination – about 80 million $m^3$/day worldwide [4],

containing about 5.6 million tonnes of salt per day (2000 million - tonnes/yr). This amount is some 8 times the current annual world salt production of 250 million tonnes/yr [5].

Ocean disposal of brine may disturb ecosystems and contributes to gradual build up of salinity in semi-closed seas like the Mediterranean, the Red Sea and The Gulf. To mitigate such environmental hazards, careful design studies have been carried out on marine outfalls, to disperse and dilute the brine as effectively as possible [6]. Nevertheless, to achieve nearly complete (99%) protection of marine species would require very large dilution factors of brines, as high as × 50 in some cases [7].

Although most desalination capacity is installed at the sea coast, a significant number of plants are installed inland to treat brackish ground water or surface water. For these inland plants, brine disposal is especially problematic: common solutions include discharge to waste-water networks or reinjection to aquifers. The former solution puts an extra load on wastewater treatment plant and the latter contributes to salinization and deterioration of aquifers [8].

Processes for recovering salts and other commodities from desalination brines are well known and demonstrated. A detailed economic study by Shahmansouri et al. [3] showed that extraction of sodium chloride, chlorine, bromine, calcium carbonate, potash, sodium hydroxide, magnesia, and rubidium are all potentially viable. The value of sodium chloride is very dependent on its purity [3]. (Thus most high-quality sodium chloride is produced from sodium mining, because mined brines are typically purer than those derived from seawater [5]). The study found, however, that the economic viability of extracting commodities from desalination brine is quite marginal in most cases – such that it is unlikely to become popular unless the avoided environmental costs of the brine disposal are accounted for.

An important exception to the general picture is the combined desalination-salt production plant at Eilat, operated by the Mekerot Water Company and the Israel Salt Company, which in 2007 produced daily about 10,000 m$^3$ of freshwater and 400 tonnes of salt [9]. The salt is produced by means of solar evaporation ponds. Ravizky and Nadav have described a number of challenges that had to be overcome to make this venture successful. For example, acid descalant was avoided, because it liberated carbon dioxide which in turn encouraged biogrowth in the brine. They also highlighted the importance of a mutually beneficial contract between the two companies, drawn up in 1995 [9].

Though evaporation ponds are not very common for seawater desalination plants, they have been widely used for inland plants. However, it is not often reported that the evaporites are being harvested as valuable commodities or for further processing. This may be because of the variable and uncertain composition of these evaporites, as compared to sea salt.

Processes for treating desalination brines include solar evaporation, wind evaporation, secondary reverse osmosis, forward osmosis, membrane distillation, electrodialysis and electrodialysis reversal. Each has its advantages and drawbacks. Solar evaporation, commonly held to be the most cost effective way to produce salt in hot arid climates, requires however a large land area. At Eilat, a pond area of 700,000 m$^2$ handles 5000 m$^3$/day of brine corresponding to a specific area requirement of 140 m$^2$/m$^3$ day [2]. Compared to evaporation from pure water, evaporation from seawater and brines is slower, because of the lower vapour pressure. To account for this, a correction factor of 0.7 has been applied [10]. Though a slower evaporation from concentrated brines might be expected compared to that from raw seawater, it has also been reported the difference in evaporation rate is in fact quite small [11].

Given their large area, seepage from evaporation ponds is frequently cited as a concern, calling for careful attention to installation and maintenance of liners [12]. Leakage is most likely to occur at the seams where liners are joined. Extra capacity is needed for periods of low evaporation rate due to poor weather, and to accommodate rainfall without overflow. Other considerations for evaporation pond design include the effect of wave action (to absorb which sloping banks are

recommended) and the need for very accurate leveling of the pond [10].

Natural energy from the wind, as well as from the sun, can be utilised for brine evaporation and salt production. 'Wind intensified evaporation' (WAIV) using wetted plastic surfaces has been trialled in the Negev [8,13]. The upright surfaces allow a 6-fold reduction in land footprint per m$^2$ of evaporative surface. Comparing to standard evaporation ponds, Katzir et al. reported a cost saving using WAIV of 20,000–40,000 euros/yr in brine disposal costs for a desalination plant producing 2400 m$^3$/day of water.

While solar and wind evaporation are almost free of energy costs, industrial processes like membrane distillation, electrodialysis and vacuum crystallization are more capital and energy intensive. Energy consumption per tonne of salt produced has been quoted in the range of 500–900 kWh/tonne in treatment systems using pre-treatment by electrodialysis to handle coal-mine brine [14]. Nonetheless, industrial processes can provide a superior range and quality of products; for example, Fernández-González et al. recently demonstrated the possibility of producing pure and concentrated hydrochloric acid from desalination brine in a system using a bipolar electrodialysis membrane [15]. Most culinary salt is produced, in its final stages, by energy intensive vacuum evaporation and crystallization processes that are favoured to achieve pure and well-formed crystals [5]. It is interesting to note that a 20% reduction in process energy was reported in electrodialytic salt production when fed with desalination brine instead of raw seawater [16].

The value chain based on desalination could be extended further by adding value to the salt produced. Salt can be upgraded for culinary and gourmet markets. Most importantly, salt is deemed the 'best vehicle for adding iodine' [17]. Iodine is an essential micronutrient, deficiency of which results in abnormal thyroid function, hypothyroidism and goiter [18]. About one third of households worldwide lack access to adequately iodised salt, and low-income countries are particularly prone to this problem. According to Andersson et al. [18]:

> Low iodine intake is the most common cause of preventable mental impairment worldwide, which is why there is a global drive to eliminate iodine deficiency through the highly effective strategies of salt iodisation and iodine supplementation.

Though the technology for iodizing salt is well known and inexpensive, significant barriers to its use in some countries include: lack of high-quality salt manufacturing and packaging techniques, and lack of regulatory systems to ensure accurate labeling and consumer confidence [17]. Risk of iodine deficiency is increased in land-locked countries due to lack of sea-derived products in the diet that may supply sufficient natural iodine.

Motivated by the environmental impact of desalination brines, the limited instances of recovery of salt and minerals from it, and by the opportunities to add value and benefits to such products, this paper investigates a new option for management of desalination brines by seawater greenhouses. The seawater greenhouse is a concept introduced in Tenerife in 1993 [19] by Seawater Greenhouse Ltd. and currently taken up by several companies including Sundrop Farms and the Sahara Forest project. The main feature of the concept is the use of seawater for evaporative cooling of a greenhouse, combined with desalination technology powered at least partially by renewable energy. Initially, seawater greenhouses were not taken up commercially due to cost and investment barriers, but this situation is now changing with the scale up to 20 ha by Sundrop Farms in Australia. The company is forecasting the production of 15,000 tons of tomatoes a year [20].

Like WAIV, the proposed concept will use wind to evaporate water and concentrate brine, but the additional value (described as 'vapour value' [21]) is in the cooling developed behind the evaporator pads and the benefit for crop cultivation and water saving in irrigation. The variant of seawater greenhouse studied here is designed for low-cost implementation using shade nets and, unlike most evaporatively-cooled

greenhouses, the system will be wind driven avoiding electricity consumption by fans.

The objective of this study is to assess this proposal with regard to two main aspects:

1. The amount of brine disposed of, and amount of salt produced, per area of evaporator pad and per area of land occupied by the system
2. The climate conditions (solar radiation, temperature, humidity and air speed) achieved in the shaded cultivation area downstream of the evaporator

In this paper, these aspects will be studied in the context of three cases studies of use in hot regions, showing options for utilisation with various brine concentrations and climate conditions. The case studies will be used to illustrate predictions from the model and make a preliminary assessment of its economic advantages. The effect of design parameters on the results will be explored. As the case studies refer to proposed future installations not yet realised, validation of the model is carried out by other means, namely: by comparison against flow over a backward-facing step (which is a reference case often used in computational fluid dynamic work), comparison against results reported in the literature relating to the shade net, and by comparison against ground temperature measurements obtained by remote sensing.

## 2. Concept

Fig. 1(a) shows the basic concept of the wind-driven seawater greenhouse. The shade-net construction has been chosen for low cost. Shade nets are already widely used for cultivation of bananas, peppers and other crops in hot climates [22,23], but not in combination with evaporative cooling pads. The dimensions shown in the Figure are parameters that will be varied in the modelling study. Nominal values of these parameters are initially defined as: overall height $H_{net} = 3$ m, overall length $L_{net} = 20$ m, and shade net porosity $\phi = 50\%$. Further nominal parameter values are included in Table 1. The seawater greenhouse reduces the brine volume and, as shown in Fig. 1(b), is combined with evaporation ponds to provide potentially a ZLD system. For salt production purposes, these ponds will be arranged as a cascade,
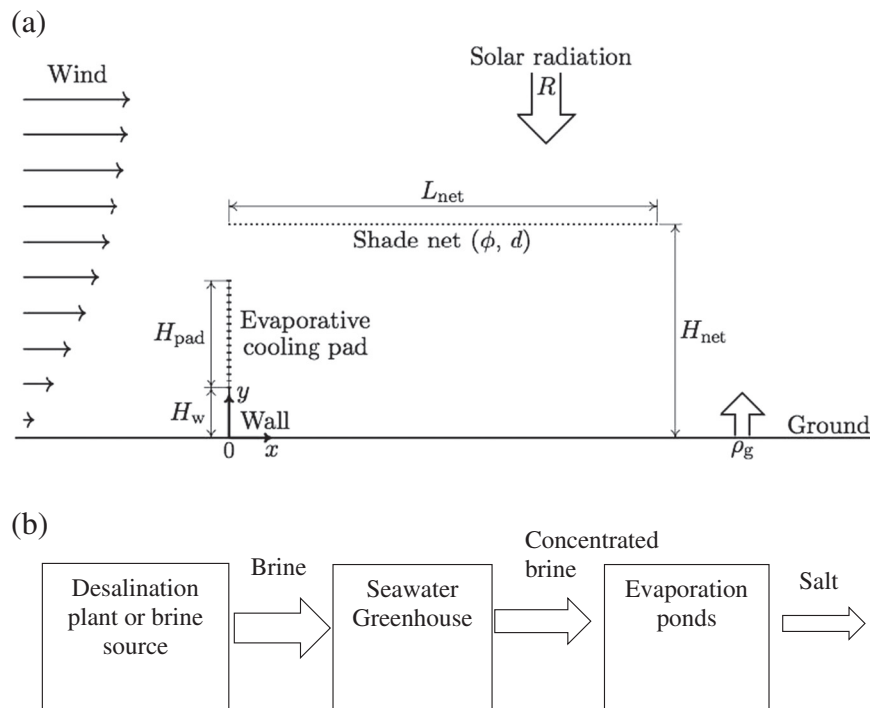
**Table 1**
Nominal values of modelling parameters.

| | | |
|---|---|---|
| Evaporative cooling pad | Height $H_{pad}$ | 1.5 m |
| | Thickness | 0.1 m |
| | Width | ∞ |
| | Bottom wall height $H_w$ | 0.5 m |
| Shade-net greenhouse | Height $H_{net}$ | 3 m |
| | Length $L_{net}$ | 20 m |
| | Width | ∞ |
| Shading net | Geometrical/optical porosity $\phi$ | 50% |
| | Hole diameter $d$ | 3 mm |
| Ambient conditions | Wind velocity range | 0–10 m/s |

allowing first calcium carbonate and calcium sulphate to precipitate at concentration factors up to about 12, with the brine then flowing into secondary ponds where it will be concentrated further for production of salt containing mainly sodium chloride.

The results of the modelling will include the evaporation rate, potential salt production rate, and internal conditions achieved. These will depend not only on the model parameters but also on the ambient conditions of temperature, humidity, wind speed and direction, and on the solar radiation received. These ambient conditions will be based on the three case studies described below. Table 2 summarises the climatic conditions for each case study locations, classified as either hot desert (DWh) or hot semi-arid (BSh) according to the Köppen system. For all locations, we use land-based data from the National Oceanic and Atmospheric Administration (NOAA), as the NOAA not only provides access to many stations all over the world, but also stores regional hourly data, of reasonable accuracy, over long periods of time [24].

## 3. Case studies: background information

### 3.1. Horn of Africa: Berbera

The Horn of Africa comprises four countries: Djibouti, Eritrea, Ethiopia and Somalia. Somalia is not a single political entity but comprises several political and tribal subdivisions, in particular the self-declared state of Somaliland. Somalia was, in the 1930s, home to the world's largest salt works at Hafun, subsequently destroyed in WW2 in

**Fig. 1.** Basic concept of seawater greenhouse for brine utilisation: (a) Seawater greenhouse with wind approaching from the left, described by a power-law velocity profile $u / U_{ref} = (y / Y_{ref})^{1/7}$ [37], where $U_{ref}$ is the reference wind velocity at height $Y_{ref} = 10$ m. The relatively dry ambient air impinges on an evaporative cooling pad, of height $H_{pad}$, elevated above the ground by a portion of solid wall height $H_w$. Downstream of the cooling pad, the cultivation area is covered by a shade net, with holes of diameter d and porosity $\phi$, positioned at height $H_{net}$ above the ground of reflectivity $\rho_g$. (b) The seawater greenhouse receives brine from a desalination plant (or other saline source) used to moisten the evaporative cooling pad over which the brine is recirculated. Hence the brine becomes more concentrated and is finally supplied to a series of evaporation ponds where salt is produced.

**Table 2**
Summary of climate conditions and data sources relating to the three case studies. Berbera: (2005–2006), Ahwaz: (2006–2015), Ahmedabad: (2006–2015). Temperature data is averaged from data from NOAA [24].

| Location | Berbera, Somaliland | Ahwaz, Iran | Ahmedabad, Gujarat |
|---|---|---|---|
| Köppen climate | Hot desert, DWh | Hot desert, DWh | Hot semi-arid, BSh |
| Coldest month | January | January | January |
| Average daily min temp (°C) | 24.7 | 7.7 | 12.7 |
| Hottest month | July | August | May |
| Average daily max temp (°C) | | | |
| Dry bulb | 42.3 | 46.3 | 42.1 |
| Wet bulb | 25.8 | 23.7 | 24.2 |
| Rainfall (mm/yr) | 51.2 [25] | 209.2 [26] | 750.9 [27] |

1941. The arid climate and current agricultural practices of Somalia limit agricultural productivity to about 0.5 tonnes/ha. Despite the arid climate, agricultural land compromises an estimated 70.3% of Somalia's land but only 1.8% of the land is cultivated with very few arable crops. Currently, Somalia and Somaliland have no significant desalination plants and in general very little industry of any kind. Their largest economic activity is the raising of livestock which accounts for 40% of GDP and for 50% of export earnings [28].

Ethiopia is a land-locked country, which has one of the highest incidences of iodine deficiency worldwide [29]. Due to the growing horticultural sector in Ethiopia, and the on-going conflict with Eritrea, access to the sea port at Berbera via Somaliland provides an essential trade route for Ethiopia.

Because of the precarious socio-economic and nutritional conditions in the Horn of Africa, it receives substantial foreign aid interventions intended to stabilize and improve conditions. With relevance to the current study, the UK's Department for International Development is sponsoring a project under the Innovate-UK Agri-Tech Catalyst Programme, to promote sustainable intensification of agriculture using seawater greenhouses in coastal areas of Somaliland [29]. The climate of Somaliland is classified as hot desert climate (Koppen-Geiger DWh). Average highs vary from 29 °C in December–January, to 41–42 °C in June–July; and average lows from 20 °C in December–January to 31 °C in July–August. Average annual precipitation in Berbera is only about 50 mm. Like other countries in the Horn of Africa, Somaliland and Somalia are very vulnerable to iodine deficiency: according to the Iodine Global Network scorecard there were, in 2014, some 435,000 infants in Somaliland with inadequate protection against iodine deficiency [30].

Under the UK-funded programme, the seawater greenhouse will be integrated with a desalination plant to provide irrigation water. It is assumed here that the brine will be at concentration of 7%, corresponding to 50% recovery ratio by the desalination plant. The system will also produce salt using an arrangement similar to Fig. 1(b). A coastal site close to Berbera has been chosen for this case study.

Quality of weather data for the Horn of Africa is generally poor; however, two good years of weather data were recorded for 2005–6 at Berbera airport, close to the intended site of construction, providing measurements at typically 4 hour intervals with 740 time points in total.

### 3.2. Gotvand Dam: Ahwaz

Iran's Upper Gotvand Dam project on the Karoun River was completed in 2013. Downstream of the dam, the Karoun traverses the Khuzestan plain which is an important agricultural area. Due to salinization of water in the dam reservoir, the river is also becoming saline, leading to degradation of land and loss of fertility in irrigated areas of the Khuzestan plain. Saline and sodic water damages soil structure and impairs the ability of crops to take up adequate water.

According to Mahjoob Farshchi et al. [31], the increasing salinity is due to the presence of a geological formation containing halite, 120 m high and extending 120 m along the bank of the reservoir. The volume of halite outcrops is estimated at 150000 m$^3$. Salt from the outcrops is gradually leaching into the reservoir. Salinity in the reservoir is stratified and reaches 14% total dissolved salts at its floor – about 4 times the concentration of normal seawater.

Management of saline water from the Gotvand dam is a major challenge, with similarities to management of brine from desalination plants. So far no practical solution has been found. Seawater greenhouses are considered here as an option for utilising this water. Its salinity will depend on the manner of extraction from the reservoir, and here is assumed to be 7% salt. The town of Ahwaz has been chosen, as it is located downstream of the dam and adjacent to the agricultural area, with good availability of weather data.

### 3.3. Gujarat: Ahmedhabad

The state of Gujarat is the largest salt-producing region of India, accounting for about 76% of the country's salt production; and it is the second largest salt exporter worldwide [32]. The dry and sunny climate of Gujarat is very suitable for salt production in solar evaporation pans along the coast and inland (Table 1). Several inland surface and groundwater saline source are exploited for this purpose. Salt production in India is generally labour intensive, employing an estimated 100,000 salt workers, known in Gujarat as 'agariyas'. These are migratory workers whose livelihood is governed by monsoon rains: they work mainly desert area of the Rann of Kutch during the manufacturing season and retreat to the surrounding villages during the monsoon. Many hardships face the agariyas: ineffective health and safety legislation, absence of workplace inspectors, occupational health hazards including gangrene and blindness, lack of access to healthcare, and non-recognised identity. Further, unseasonal rains can wash away their salt pans and temporary dwellings [33]. Andharia [33] cites Tata Chemical Industries as an example of an organization that is taking very positive steps to provide improved conditions for salt pan workers, including health check-ups, training in first aid, and provision of a free hospital.

Through companies such as Tata Chemicals, Gujarat Alkalies & Chemicals, and Reliance Industries, Gujarat has a modern chloroalkali industry based on sea salt. This is supported by the government-funded and well equipped Central Saline and Marine Chemicals Research Institute at Bhavnagar. Gujarat has several large-scale desalination plants installed, including the 150,000 m3/day and 65,000 m3/day MED plants of Reliance and Essar respectively, at Jamnagar, commissioned in 2008 and 2012 [34].

Gujarat is among the driest states of India: though home to 5% of Indians it has only 2% of water resources occurring mainly during the monsoon. The rainfall is variable over the state, the most arid region being that of Kutch, which has no perennial rivers [35]. Given the growing populations, increased installation of desalination plants can be anticipated. For this study, the city of Ahmedabad has been chosen for the case study location, due to the good availability of weather data. It is located about 100 km from the Kutch region.

The fraction of households using adequately iodised salt in Gujarat is about 70% [36]. As pointed out by Yadav et al. [37], inadequate iodisation is common in small scale salt production, which represents about 30% of salt production in India. This is attributed to limited access to know-how and inadequate laboratory facilities among the small-scale salt producers.

## 4. Modelling

The conditions inside the seawater greenhouse are studied based on a thermal-fluid dynamic approach. The fundamental equations used are the incompressible Navier-Stokes equations:
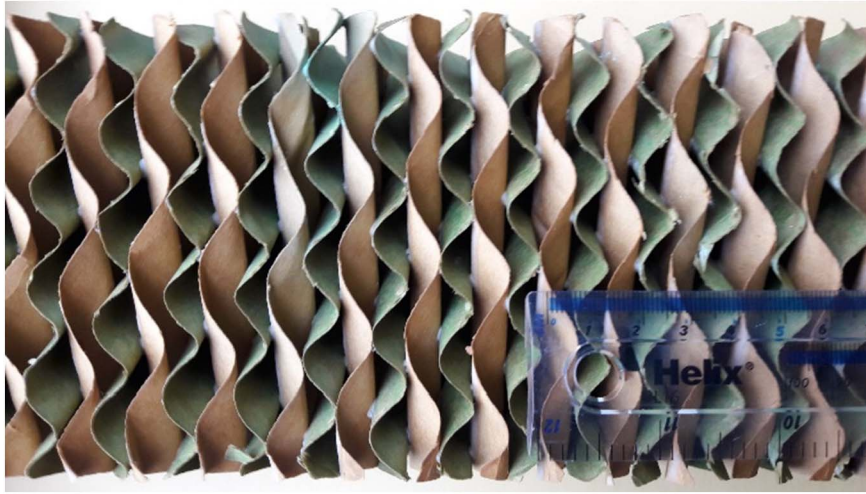
$$\nabla \cdot \boldsymbol{u} = 0, \tag{1}$$

$$\rho \left[ \frac{\partial \boldsymbol{u}}{\partial t} + (\boldsymbol{u} \cdot \nabla) \boldsymbol{u} \right] = -\nabla p + \mu \nabla^2 \boldsymbol{u} + \boldsymbol{f}, \tag{2}$$

and transport diffusion equations for the temperature T [°C] (i.e. energy equation):

$$\rho c_{\mathrm{p}} \left[ \frac{\partial T}{\partial t} + (\boldsymbol{u} \cdot \nabla) T \right] = \lambda \nabla^2 T, \tag{3}$$

and for the water vapour concentration $w$ [kg/m$^3$]

$$\frac{\partial w}{\partial t} + (\boldsymbol{u} \cdot \nabla) w = D_{\mathrm{w}} \nabla^2 w, \tag{4}$$

where $t$ [s] is time; $\mathbf{u}$ [m/s] and $p$ [Pa] are the velocity vector and pressure respectively; $\rho$ [kg/m$^3$], $\mu$ [Pa·s] and $\lambda$ [W/m·K] are the density, viscosity and thermal conductivity of the air respectively; and $D_{\mathrm{w}}$ [m$^2$/s] is the diffusion coefficient of water vapour in air. We used a constant value: $D_{\mathrm{w}} = 2.60 \times 10^{-5}$ m$^2$/s at $T_{\mathrm{db}} = 298$ K and ambient pressure 1013.25 hPa [38]. The buoyancy effect due to variations in temperature and humidity is taken into account by the vertical force vector $\boldsymbol{f}$ per unit volume of fluid [N/m$^3$] using a modified Boussinesq approximation

$$\boldsymbol{f} = \rho \boldsymbol{g} = \rho_0 \boldsymbol{g} \left[ 1 - \beta \Delta T - \gamma w \right], \tag{5}$$

where $\rho_0$, $\boldsymbol{g}$, $\beta$, $\Delta T$, $\gamma$ and $w$ are reference density, gravity vector, thermal expansion ratio [1/K], temperature difference from reference temperature $(T - T_0)$, air exclusion ratio by water vapour $\gamma = (\frac{11}{18\rho_0})$ [m$^3$/kg] respectively.

The equations are solved numerically, via a finite difference method based on a Large Eddy Simulation [40,41]. The modelling approach is essentially a two-dimensional one, because the greenhouse structure is intended to extend for a large distance in the span-wise direction compared to the stream-wise distance $L_{\mathrm{net}}$, thus resulting in a translational symmetry. This assumption is justified by the fact that the structures are being designed to cover large areas (i.e. several hectares), such that end effects would only affect relatively small portions. As shown in Fig. 1(a), $x$, $y$ coordinates are used to represent the stream-wise direction $x$, and vertical direction $y$.

Before applying these equations to the whole domain of the seawater greenhouse, we consider separately the key components, namely the evaporative cooling pad and the shade net, to determine quadratic pressure drop coefficients C according to:

$$\Delta P = \frac{1}{2} \rho C \, |u| \, u, \tag{6}$$

where $\Delta P$ and $u$ are respectively the pressure drop across the medium

and the velocity through the medium. The quadratic pressure drop coefficient enables these components to be represented simply in the overall model, without the need to model very small-scale features at the level of the pores. Initial modelling regarding each of these components in isolation is carried out to provide useful results prior to the modelling of the whole system. In the case of the evaporative cooling pad, pressure drop C is well characterised and can be determined from manufacturers' data (Appendix A). Since the flow field in the wake of the evaporative cooling pad is considered not to affect significantly the flow rate through the pad, a study of the pad in a free flow field is useful to determine evaporation rates. It is shown that the air flow through the pad provides a nearly constant wind reduction factor which can be applied over a time series of wind velocities to determine cumulative evaporation rates. In the case of the shade net, commercial information on pressure drop is not readily available; instead this component is modelled in detail to determine a value of C. For both of these initial models, direct numerical simulation (DNS) was used for greatest accuracy – avoiding the need to introduce turbulence models. However, DNS was not practical for modelling of the whole system and thus a turbulence model and use of a wall law was introduced (as described in Section 4.3). In all cases, bespoke FORTRAN code was created to solve the equations.

### 4.1. Evaporative cooling pad

The evaporative cooling pad is an essential part of the seawater greenhouse. As seen in Fig. 2, the pad has a wavy structure with a pitch of 7 mm between pitch and summit. The wet evaporative pad releases water vapour, when wind penetrates the pad through the gaps. Pressure drop and evaporative efficiency data, as provided by the manufacturers [39], are used to calibrate our model in which the pad is simplified as a uniform porous medium. A quadratic resistance was found appropriate, where the pressure drop is proportional to the square of the mean normal velocity (Eq. (6)), and determined to be $C = 14.4$ for values of $u_{\mathrm{pad}}$ up to 20 m/s with pad thickness 0.1 m. See Appendix A for further details.

For a general prediction of flow through the evaporative cooling pads, the pad was modelled in a free air flow (with no ground friction) and choosing a pad height of 3 m. This excess height was chosen to be much larger than the thickness of the pad, specifically to study the end effect in a very tall pad, with the hypothesis that the end effects may be small (as will be verified later). Based on solution of Eqs. (1) and (2), modelling of this flow field around the pad is depicted in Figs. 3(a) and 3(b) for a perpendicular wind velocity $U_0 = 1$ m/s.

Note that in this case the flow field is isothermal and constant density: Eqs. (3)–(5) are not needed. Instead, the body force $\boldsymbol{f}$ is based
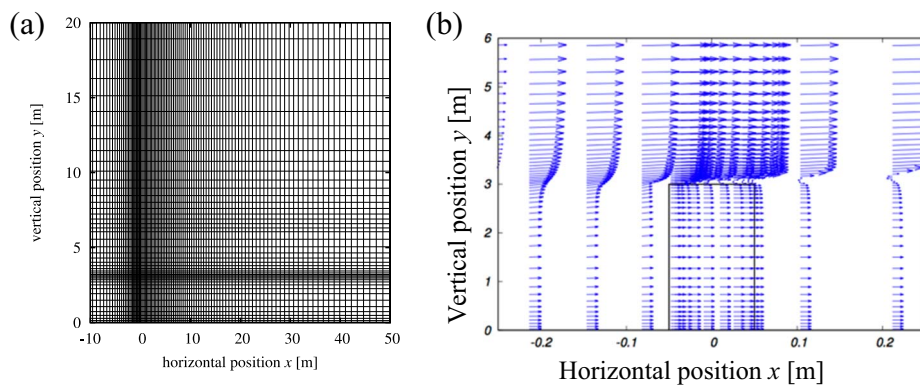
**Fig. 3.** Air flow through the evaporative pad in absence of ground friction: (a) computational grid points around and inside evaporative cooling pad ($|x| < = 0.05$ m). The grid is designed to have closer spacing near the edges of the pad, by using hyperbolic tangent mappings. Total numbers of grid points: $N_x = 275$, $N_y = 100$. (b) Resulting velocity field $u$ for $U_0 = 1$ m/s, pad height 3 m and thickness 0.1 m.

on a quadratic resistance per length corresponding to Eq. (6): $f = -\frac{1}{2}\chi\varrho |u| u$, where $\chi = 144$ m$^{-1}$. As this is a 2D model, the pad is extended infinitely in $z$, and the origin of the coordinate system is at the centre of the pad in this case. The computational domain is $100 \times 60$ m$^2$ in the $x$ and $y$ directions, respectively, with the pad 20 m downstream of the flow inlet.

Fig. 3(b) shows velocity vectors $u = (u,v)$ enlarged around the pad on the $x$-$y$ plane. The magnitude of the normalised velocity vector, $|u|/U_0$, is depicted in Fig. 4, where $|u| = \sqrt{u^2 + v^2}$. The ratio of the velocity through the pad ($u$) to the ambient velocity ($U_0$) is thus determined to be $|u|/U_0 \sim 0.31$ for $|y|/H < 1$.

For $H = 3$ m and wind velocity $U_0 \leq 10$ m/s there was found to be almost no difference in the velocity profile $u/U_0$ over the pad as shown in Fig. 3(b), such that the velocity reduction factor 0.31 is considered to be generally applicable independent of dimensions and wind speed (see Fig. 4). This factor applies to over the whole flow field leaving the pad, except for a small region at the tip of the pad as shown in Fig. 3(b).

To confirm the validity of the use of the constant velocity reduction factor, modelling was carried out with the evaporative cooling pad incorporated in the greenhouse structure, for the case study of Ahmedabad (May conditions) – following the method of Section 4.3. As shown in Fig. 5, variations in pad height result in only a $\pm$ 10% variation in exiting velocity averaged over the pad height. Temperature and humidity are also seen to be substantially uniform at the exit. Based on the ambient conditions for the site, we therefore use the velocity reduction factor to predict the amount of evaporation per m$^2$ of pad according to the surrounding condition, namely the dry-bulb temperature ($T_{db}$), humidity and wind velocity and direction only. The evaporation is assumed to be independent of the shade net arrangement
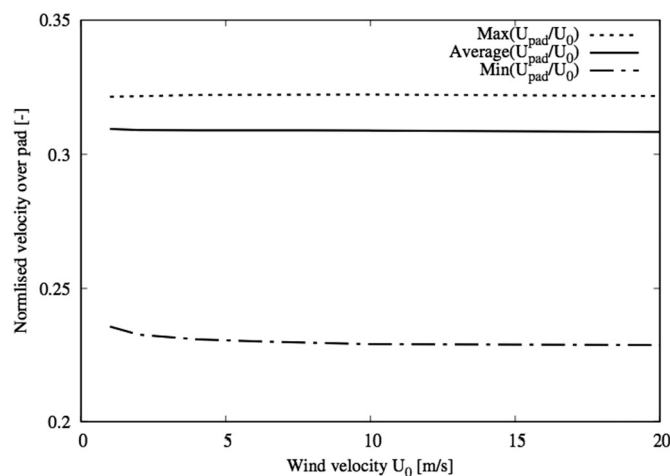
downstream and of the solar radiation intensity. The procedure is as follows:

1. Calculate the velocity of flow through the evaporative cooling pad based on the normal component of wind speed and on the velocity reduction factor (having value of 0.31 as shown in Fig. 4 for the 0.1 m thick pad).
2. Using psychrometric relations (Appendix B), calculate the maximum potential increase in $w$, based on ambient absolute humidity at inlet and corresponding wet-bulb conditions at outlet, corresponding to an ideal 100% saturation efficiency of the pad.
3. To determine the actual increase in $w$, multiply this maximum increase by the saturation efficiency $\eta$, as determined from velocity $u_{pad}$ at the pad by Eq. (7) below derived by fitting to the manufacturers' data:

$$\eta = 0.955 - 0.185 (u_{pad})^{0.452} \tag{7}$$

(for thickness of pad $t_{pad} = 0.1$ m). Thus we determine $w$ at the outlet of the pad, and the corresponding evaporation rate. Detailed psychrometric relations are included in Appendix B.

### 4.2. Shade net

The shade net structure is modelled by a thin film, where the film has circular holes of diameter $d = 3$ mm uniformly placed on square grid points (Fig. 6) at pitch $L_x = L_z = 3.76$ mm, so as to provide 50% overall porosity. This pitch and porosity is fairly typical of that used in real nets. Though the geometry used in the model is somewhat simplified, the porosity is believed to be the important parameter. The flow field is assumed to be symmetric about the four symmetry planes of the square grid. The pressure drop coefficient for the net is obtained by the following procedure, considering the net to be placed in normal velocity field with bulk velocity 1 m/s. Unlike in Sections 4.1 and 4.3, in this case the model is a 3D one.

The net resistance against the air flow has the effect of lowering the static pressure, even though the velocity is recovered downstream of the net. We see this effect by depicting the stream-wise component of the velocity and the pressure along an axis passing through the centre of the holes, as a function of distance from the hole, as shown in Fig. 7(a) and (b) for uniform flow field approaching at 1 m/s. Once we know the relationship between the uniform flow speed and the pressure drop, then we can predict the pressure drop for any speed of the uniform flow under the quadratic resistance approximation of Eq. (6). Note that there is a wake region behind the net, extending about 0.1 m. As the scale of the whole greenhouse model is much larger than 0.1 m, we base the calculation of pressure drop on conditions downstream of this region, resulting in a value of pressure drop coefficient of C = 3.67 as obtained by matching Eq. (6) to the results of the DNS at approach velocity of 1 m/s.

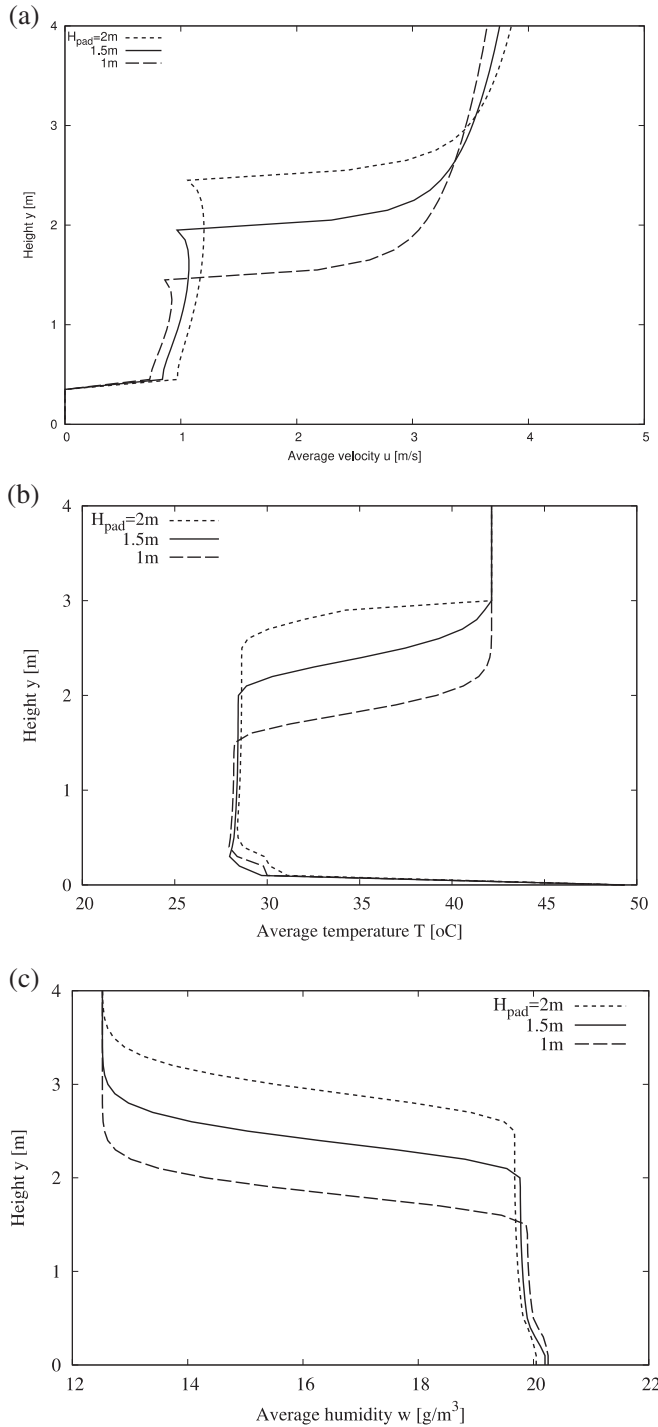To check grid convergence of the computation, the velocity at the



**Fig. 4.** Average velocity through pad ($x = 0$), the minimum and maximum velocity normalised velocity through the pad $u_{pad}/U_0$. The pad thickness and height are 0.1 m and $H = 3$ m, respectively.

**Fig. 5.** Results of computations confirming that the behaviour of the exit conditions immediately downstream of the evaporative cooling pad are substantially independent of vertical position $y$ and pad height $H_{pad}$: (a) horizontal component $u$ of velocity vector; (b) temperature $T$ and (c) humidity $w$. Here the pad is mounted on a solid wall 0.5 m high, and subject to an ambient wind speed of 3.7 m/s. Three pad heights are modelled: 1, 1.5 and 2 m. The parameters on the abscissae of the graphs are time averages.

centre of the holes against number of grid points is shown in Fig. 8, where $N_y$ corresponds to half of the grid points on the centre line of the holes normal to the net. On this basis, simulations are carried out with $N_y = 480$, $N_r = 80$, and $N_\theta = 10$.

## 4.3. Modelling of whole greenhouse

The modelling of the whole greenhouse shown in Fig. 1 was achieved by solution of the Navier-Stokes and transport diffusion equations for temperature and humidity over a rectangular computational domain including the greenhouse, of 100 m longer than the greenhouse length (36 m upstream and 64 m downstream) in the stream wise ($x$) direction, and 30 m in height (vertical direction, $y$). A uniform square grid was taken, and the size is 0.025 m with a time step of 1 ms. The equations were spatially discretised based on a finite difference approximation, and the thermal and flow fields were developed by using simplified mark and cell method (SMAC) [42,43]. The KK-Scheme [44] and 4th order finite difference approximation were adopted for advection and diffusion terms, respectively. A second order Adam-Bashforth scheme was selected for the integration with respect to time.

Boundary conditions were defined as follows. The wind (blowing from the left) is described by a power-law velocity profile as in [45].

$$u/U_{\mathrm{ref}} = (y/Y_{\mathrm{ref}})^{1/7}, \ v = 0, \tag{8}$$

where $U_{\mathrm{ref}} = U_0$ is wind velocity at reference height $y = Y_{\mathrm{ref}} = 10$ m corresponding the meteorological input data. The boundaries of the computational domains were: at the left, according to this velocity profile; upper boundary, constant velocity and constant humidity w ($v = 0$, $u$ according to Eq. (8), w according to the ambient conditions); to the right by a Sommerfeld boundary condition.

$$\frac{\partial \psi}{\partial t} + c \frac{\partial \psi}{\partial x} = 0, \tag{9}$$

where $\psi$ can represent $u$, $T$, or $w$; and $c$ is the phase velocity at the right boundary, approximated by the horizontal velocity component $u$ estimated at the grid point preceding the boundary. However, $c$ is constrained to values $\geq 0$ in order to avoid the need to extend the computational domain downstream, by disallowing propagation of flow properties upstream across the boundary. A constant pressure was imposed at the right boundary.

In the region of the solid boundary at the ground, velocity changes are very rapid, potentially requiring an impractically large number of grid points in the finite difference scheme. To avoid this problem, instead of using a simple non-slip boundary condition, use is made of the Spalding law [46]:

$$u^+ = y^+ + e^{-5.5\kappa}\left[e^{\kappa u^+} - 1 - \kappa u^+ - \frac{(\kappa u^+)^2}{2} - \frac{(\kappa u^+)^3}{6}\right]. \tag{10}$$

Herein dimensionless parameters are defined $u^+ = \frac{u}{u_\tau}$, $y^+ = \frac{u_\tau y}{\nu}$. And $u_\tau$ is the friction velocity at the ground, $\nu$ is kinematic viscosity and the Karman constant $\kappa$ is assumed to be $\kappa = 0.41$, as found in experiments for a smooth wall [47,48]. Similar wall functions are used to represent tangential velocity components in the vicinities of the vertical evaporator pad and the shade net.

Special attention was paid to the thermal boundary conditions at the ground, as described next, whereas a zero-flux boundary condition is assumed for humidity field $w$. This assumption is made on the basis of dry ground, with no evaporation, which would be typical of desert locations – and allows the model to be applied generally without assumptions specific to the location.

### 4.3.1. Estimation of solar radiation

For the sites of interest, direct measurements of solar radiation where not available, therefore a model had to be used based on assumed clear sky conditions. This is justifiable since we are mainly interested in predicting maximum values of temperature typically corresponding to such conditions. The intensity of direct solar radiation at the ground is estimated using an approximate fit of normal incidence radiation $R_d$ [W/m$^2$] for a clear sky condition as a function of air mass $AM$, as provided in Fig. 3.2 of Sorensen [49]:
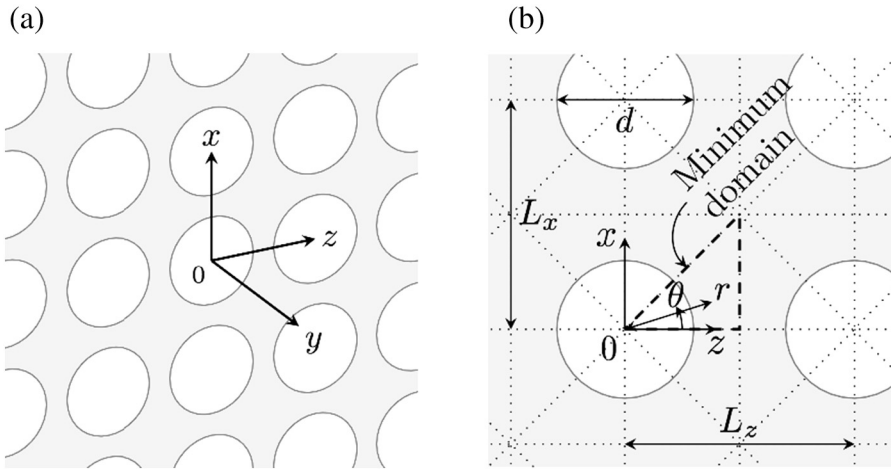
**Fig. 6.** Geometric model of shade net for pressure drop determination showing (a) local co-ordinate system and (b) symmetry planes (dotted lines) used to simplify modelling.

$$R_d = 948.2 \exp[-0.314 \, AM] + 151.7, \tag{11}$$

where $AM = 1/\cos(\zeta)$, and $\zeta$ is the zenith angle. So $R = R_d \cos(\zeta)$ was used for the solar energy that reaches to the horizontal ground.

### 4.3.2. Atmospheric longwave radiation from sky

Preliminary studies showed that the radiation balance has importance through a strong effect on the ground temperature. Based on literature the Clarke's formula [50,51] is selected as the preferred model which predicts the sky temperature $T_{sky}$ by.

$$T_{sky}^4 = \left\{ 9.366 \times 10^{-6}(1 - CC) T_{db}^6 + T_{db}^4 CC (1 - 0.84 CC) \left[ 0.527 \right. \right.$$
$$\left. \left. + 0.161 e^{8.45\left(1 - \frac{273}{T_{db}}\right)} + 0.84 CC \right] \right\}, \tag{12}$$

where $CC$ is cloud coverage ranging between 0 and 1. For a clear sky ($CC = 0$), and then $T_{sky}$ is a function of the ambient temperature $T_{db}$ only:

$$T_{sky}^4 = 9.366 \times 10^{-6} T_{db}^6. \tag{13}$$

### 4.3.3. Optical property of shade net

An analytical approximation to this energy balance is used as follows. The optical shade net is assumed to have transmittance equivalent to its porosity $\phi$, and reflectance $\rho_n$ with respect to the solid fraction of the net (giving overall reflectance $[1 - \phi] \rho_n$). The ground is assumed to have reflectance $\rho_g$ and therefore absorption $(1 - \rho_g)$. Total solar energy must be split into components of ground absorption G [W/m²] and absorption by the net, and reflection to ambient. Energy balance of these quantities considering the possible multiple reflections between the ground and shade net leads to:

$$\frac{G}{R} = \frac{(1 - \rho_g)\phi}{1 - (1 - \phi)\rho_n \rho_g}. \tag{14}$$

In this application, a high value of $\rho_n$ is desirable. Optical reflectance of shade net materials can be enhanced by use of aluminium foil or polyethylene paper to > 0.6, which is the value of $\rho_n$ assumed here [52]. A reflectance value of $\rho_g = 0.3$ [53] has been used for the ground respectively giving (together with $\phi = 0.5$), a value of $G/R = 0.385$. In this absence of any net, $G/R = 0.7$.

### 4.3.4. Energy balance at ground

We assume that the solar radiation (short wave, $R$), the atmospheric radiation (long wave, $\sigma T_{sky}^4$), the thermal conduction including convection above the ground and the thermal conduction underneath the ground toward soil are balanced at the ground:

$$G + \sigma \left[ \phi T_{sky}^4 + (1 - \phi) T_{db}^4 - T_g^4 \right] + \lambda_{air} \frac{\partial T_g}{\partial y} - \lambda_{soil} \frac{\partial T_g}{\partial y} = 0, \tag{15}$$

where $\sigma$ is the Stefan-Boltzmann constant ($5.67 \times 10^{-8}$ W/m²·K⁴), $\phi$ is the porosity of netting above the ground, and the net temperature is assmed to be the ambient one $T_{db}$. Note that the temperature gradient terms must be evaluated at the air and soil sides of the ground surface respectively. The properties of material used in this study are listed in Table 3.

Calculations showed that energy storage in the ground layer had a significant effect on the ground surface temperature. To model the ground layer, the energy equation was also applied using physical properties as given in Table 3. The soil conductivity for sandy soil, typical of locations of use, was estimate at $\lambda_{soil} = 0.3$ W/m K [55,56]. Based on a preliminary calculation using an analytic solution to the semi-infinite heat conduction problem with a sinusoidally varying temperature over the day, it was estimated that the amplitude of
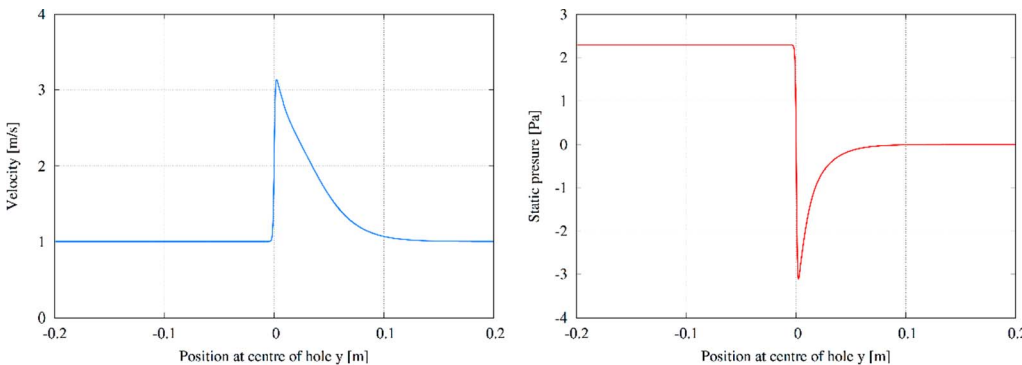


**Fig. 7.** Flow through shade net. The hole diameters are 3 mm, and the volume fraction of the net is 50%. (a) velocity and (b) static pressure at the centre of the holes. The velocity far from the net is 1 m/s in the y direction. The position of the net is at $y = 0$ and increasing $y$ is measured in the direction of flow, along an axis perpendicular to the net and passing through the hole centre.
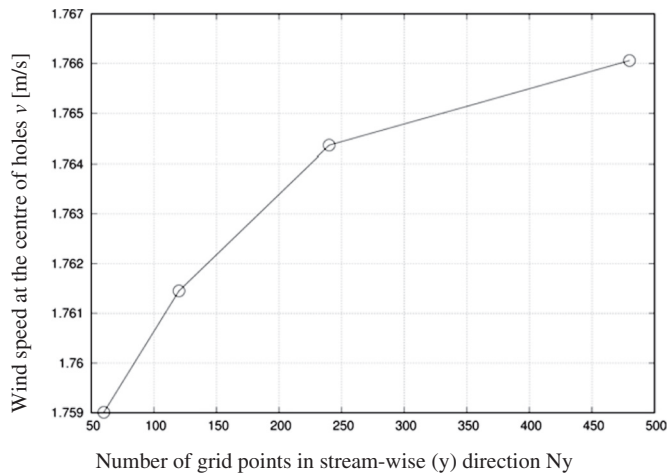
**Fig. 8.** Grid convergence. $v$ is the axial component of the velocity at the centre of holes. $2N_y$ corresponds to the number of grid points between inlet and outlet (i.e. over distance 0.4 m).

**Table 3**
Properties of materials [54,55,56].

| Material | Density | Viscosity | Specific heat | Thermal conductivity |
|---|---|---|---|---|
| | $\varrho$ [kg/m³] | $\mu$ [Pa·s] | $c_p$ [kJ/kg/K)] | $\lambda$ [W/m/K] |
| Air | 1.225 | $1.789 \times 10^{-5}$ | 1.004 | 0.0241 |
| Soil | 1560–1720 | n/a | 0.5–0.8 | 0.2–0.6 |

variation of temperature would be attenuated by 90% at a depth of 0.1 m approximately. On this basis, a boundary of constant temperature was imposed at $y = -0.1$ m.

We note also that the ground model does not attempt to take into account the effect of crops on ground temperature and airflow. The model is for dry, bare ground. Presence of crops is expected to lower temperatures, because of evapotranspiration. This approach is preferred for generality, because it avoids specific assumptions about crop types, and because it is useful to predict peak temperatures before plants are introduced or when they are at an early stage of growth.

### 4.3.5. Procedure for determining typical weather conditions for model input

For the purpose of providing information about climate conditions inside the greenhouse, it is useful to provide average daily minima and maxima for each month, as this information would be useful for growers in determining suitable types of crops and growing schedules. Rather than conduct calculations continuously over a whole year, which would be computationally too expensive, a calculation was performed based on a typical day of each month, using average daily maxima temperatures as the input boundary conditions. Monthly daily averages of dry bulb and wet bulb temperature ($T_{db}\uparrow$ and $T_{wb}\uparrow$ respectively) were determined from analysis of the raw weather data (Table 4). It was observed that weather patterns were such that these maxima typically occurred at a particular time of day for each location. For example, in Somaliland, high temperatures were observed early in the day with the wind blowing from the south before turning to blow from the north later in the day. In the other two locations, maximum temperature conditions tended to occur around noon. Dry-bulb and wet-bulb temperature tend to rise and fall in synchrony, peaking at the same time of day to within about 1 h, and thus selection of peak conditions based on dry-bulb temperature was considered satisfactory. The average time of day thus determined was used for the estimation of wind speed and direction and of humidity, also based on monthly averaging, to determine also these inputs to the model for the model. Typical input conditions thus calculated for each location are shown in

**Table 4**
Representative conditions for each month selected on basis of average daily maximum temperatures.

| Month | Time (h) | Wind speed $U_0$ (m/s)/direction (°N) | Ambient temp. dry bulb/wet bulb (°C) $T_{db}\uparrow/T_{wb}\uparrow$ | Relative humidity (%) |
|---|---|---|---|---|
| (a) Berbera (2005, 2006) | | | | |
| January | 9:27 | 4.91/229.61 | 28.36/22.93 | 62.60 |
| February | 9:38 | 5.32/241.82 | 29.17/23.75 | 63.11 |
| March | 9:21 | 5.24/208.18 | 30.51/25.45 | 66.12 |
| April | 9:32 | 5.29/244.65 | 31.27/26.11 | 65.83 |
| May | 9:43 | 5.11/255.21 | 35.92/28.01 | 53.16 |
| June | 9:56 | 7.83/222.31 | 42.14/26.12 | 25.53 |
| July | 10:40 | 10.14/226.25 | 42.31/25.82 | 24.29 |
| August | 10.31 | 8.32/230.58 | 41.58/26.03 | 26.49 |
| September | 9:55 | 6.36/255.22 | 40.37/26.48 | 30.98 |
| October | 9:24 | 5.54/256.98 | 32.72/26.44 | 60.02 |
| November | 9:40 | 4.97/260.43 | 30.86/24.79 | 60.14 |
| December | 9:22 | 4.71/266.46 | 29.83/23.98 | 60.85 |
| (b) Ahwaz (2006–2015) | | | | |
| January | 12:16 | 2.66/235.94 | 17.70/11.01 | 44.35 |
| February | 12:11 | 3.26/228.58 | 21.17/12.50 | 34.95 |
| March | 12:14 | 3.58/242.89 | 26.89/14.29 | 22.08 |
| April | 12:08 | 3.38/250.70 | 32.92/17.30 | 18.08 |
| May | 12:11 | 3.44/267.67 | 39.82/20.39 | 14.36 |
| June | 12:27 | 4.23/280.85 | 44.86/21.38 | 10.12 |
| July | 12:19 | 4.08/276.62 | 46.24/23.30 | 12.19 |
| August | 12:23 | 3.32/271.99 | 46.26/23.74 | 13.00 |
| September | 12:09 | 3.12/268.57 | 42.34/21.86 | 14.12 |
| October | 11:52 | 2.75/254.05 | 35.97/19.86 | 19.68 |
| November | 11:54 | 2.38/256.80 | 25.80/15.74 | 32.81 |
| December | 12:02 | 2.48/244.29 | 19.52/12.36 | 43.11 |
| (c) Ahmedabad (2006–2015) | | | | |
| January | 10:34 | 2.84/151.06 | 27.84/16.65 | 29.57 |
| February | 10:53 | 2.70/195.28 | 31.36/17.88 | 23.85 |
| March | 11:04 | 2.62/230.03 | 36.09/19.43 | 18.17 |
| April | 11:16 | 2.82/257.22 | 40.08/21.71 | 17.20 |
| May | 11:31 | 3.74/258.91 | 42.14/24.21 | 20.13 |
| June | 11:14 | 3.56/235.17 | 38.76/27.07 | 37.92 |
| July | 11:14 | 3.10/238.39 | 33.48/27.21 | 60.47 |
| August | 11:04 | 2.61/244.25 | 32.33/27.05 | 65.64 |
| September | 10:41 | 2.48/241.52 | 33.71/27.10 | 58.70 |
| October | 10:17 | 2.24/188.59 | 35.98/23.59 | 32.78 |
| November | 09:55 | 2.25/139.03 | 33.01/20.81 | 30.71 |
| December | 10:13 | 2.58/146.81 | 29.63/18.06 | 29.87 |

Table 4 below, as used for the prediction of peak inside temperature conditions. Meanwhile, for the prediction of evaporation rates (where the calculation was less complex and faster) round-the-clock integration was carried out, with input data provide 4 times per day for Berbera and hourly for Ahwaz and Ahmedabad.

### 4.4. Validation

To validate the software, three different approaches were used: (i) validation against a reference experimental case of the backward facing step taken from the literature, (ii) pressure drop relation through porous plate against literature and (iii) validation against ground temperature as measured by satellite.

### 4.4.1. Validation against flow over backward-facing step

The computational tool as used to analyse thermal-fluid dynamics in this paper was validated against the reference case of a standard fluid dynamics problem, the backward-step flow, for which a thorough experimental investigation has been reported [57]. As seen in Fig. 9 below, normalised velocity values agree to within 8%. One limitation of this comparison is the range of Reynolds numbers used – in the experimental case $Re = 5 \times 10^3$, the maximum covered by the reference experimental study, whereas in the greenhouse climatic model $Re$ up to $5 \times 10^5$ occur. Nevertheless, the good agreement at the lower $Re$,
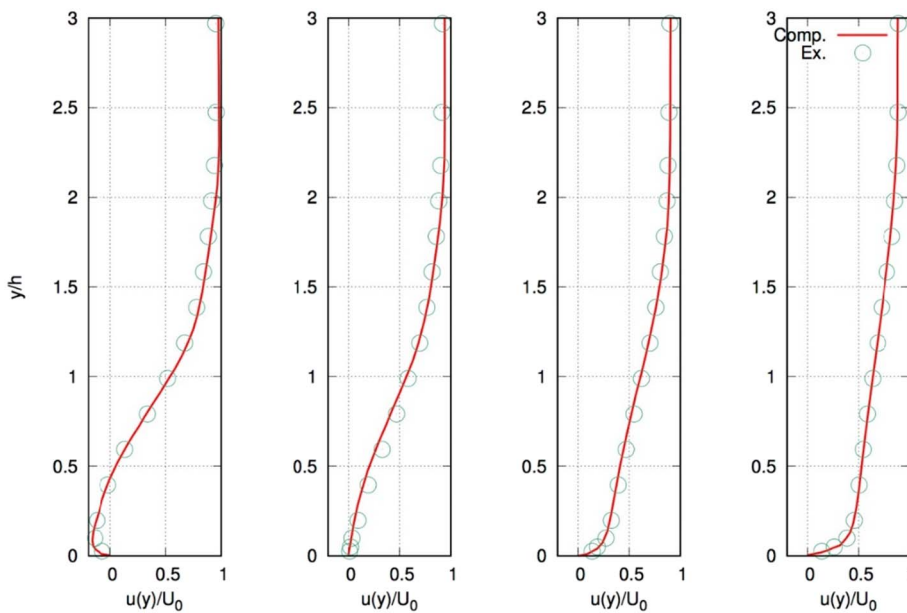
**Fig. 9.** Comparison of mean horizontal velocity profiles at four horizontal positions x downstream of a backward facing step, corresponding to normalised values x/h = 4, 6, 10 and 19 (left to right) where h is the height of the step. The comparison is made between computational values from this study (solid line) and experimental values from [57], using time average values of u normalised to the inlet velocity $U_0$.

demonstrating correct convergence of the model to the experimental results and the main implication for the higher *Re* modelling is the need for a finer grid as explained in Section 4.4.4.

### 4.4.2. Comparison with results for porous screens from the literature

A number of researchers have conducted experimental studies on porous screens using air and water. Numerical modelling studies are also reported. Table 5 below compares the current result of pressure drop coefficient of C = 3.67 against literature cases that give results varying from C = 3.18 to 4.37. Therefore, the values can be considered to be in reasonable agreement, given that the other studies have certain differences with respect to the range of *Re* covered, method of the study and shape and the exact porosity chosen, as indicated in the Table.

### 4.4.3. Validation against remote sensed data

Remote sensed data provide a potentially powerful means of validating the outputs of the model, although some simplifications have to be made in the modelling to enable a comparison with such data. The approach was to model the system as in Fig. 1(a), but simplified by removing the evaporative cooling pad and shade net. Thus we were able to compare our prediction of ground temperature ($T_g$) as appearing in Eq. (15), against remote sensed data as collected from the NASA Moderate Resolution Imaging Spectroradiometer (MODIS). This satellite instrument is flown on board two satellites, Terra and Aqua, which follow a sun-synchronous orbit, providing two readings per day. As the instruments can only measure ground temperature accurately under clear sky conditions, times of day corresponding to these

conditions were selected in order to run the computational fluid dynamic model for comparison of the ground temperature. The use of ground temperature in the model validation was justified by the fact that ground temperature is an important variable in the model, influencing the rate of heating and temperature under the shade net.

Fig. 10 shows that, in general the model prediction tends to show significantly higher ground temperatures than the satellite data, with variation in the range 0–20 °C. A straight fit on the absolute temperature scale, shows a gradient of 1.02 whereas a gradient of 1.00 would indicate identity between the predicted and satellite data. The discrepancy could be explained by a number of factors: (i) simplicity of the solar radiation model based on 'clear sky', may overpredict solar radiation due to high atmospheric turbidity or pollution; (ii) uncertainty in the soil reflectance (albedo) and variations in ground quality and coverage; (iii) ground moisture and evaporation which is not taken into account by the model.

### 4.4.4. Grid convergence

The verification of grid convergence is shown in Fig. 11; this led to a choice of grid spacing of 0.025 m for the computations applied to the whole greenhouse system.

## 5. Results

### 5.1. Evaporation and salt production

Use of the velocity reduction factor from Section 4.1 enables the

**Table 5**
Pressure drop for flow through porous screens, comparing this study with the literature.

| Study | Pressure drop coefficient C | Geometric conditions | Reynolds number *Re* and flow conditions | Thickness | Study |
|---|---|---|---|---|---|
| Present study | 3.67 | Porosity = 0.5 Diameter 3 mm | *Re* = 171 Upstream velocity = 1 m/s Density of air = 1.225 kg/m³ | Zero thickness | Computation |
| Idelchik (1996) [58] | 4.37 | Porosity = 0.5 Perforated plate | Reynolds number ≥ 10⁵ | Thickness/diameter < 0.015 | Experiment |
| Teitel et al. (2009) [59] | 3.18 and 3.63 | Porosity = 0.52 Rectangular holes (764 um × 555 µm) | Formula for upstream velocity 1 and 0.8 m/s corresponding to Reynolds numbers 37.2 and 29.8 (Density of air: 1.225 kg/m³ assumed) | Thickness/diameter = 0.24, 0.34, 0.52 | Computation |
| Guo et al. (2013) [60] | ~4 | Porosity = 0.5 Circular holes | Reynolds number ≥ 10⁵ | Thickness/diameter = 0.3 | Computation |
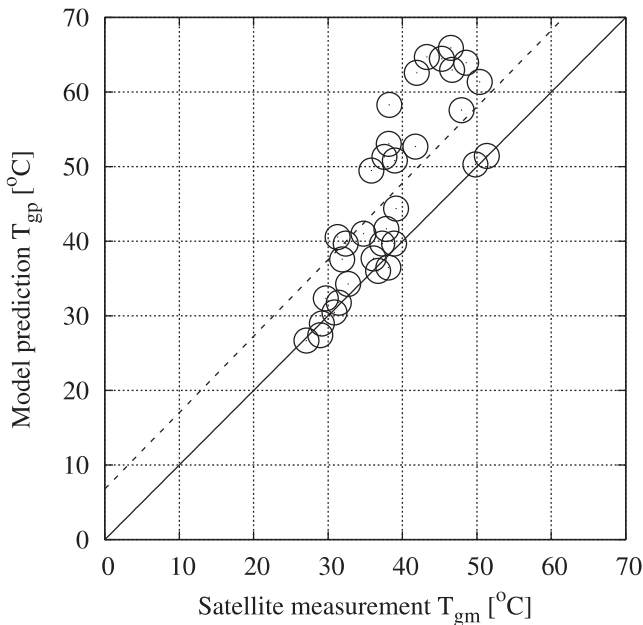
Fig. 10. A linear function, $T_{gp} + 273.15 = 1.02(T_{gm} + 273.15)$, fitting the comparison between satellite measurement data ($T_{gm}$) and the present model prediction ($T_{gp}$) for the ground temperature in Ahmedabad, India (2015).
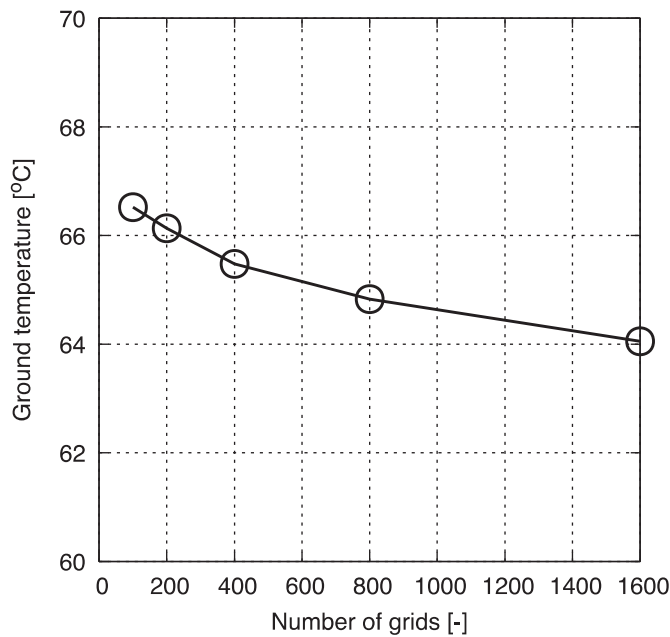


Fig. 11. Grid convergence of ground temperature with respect to number of grids in the vertical direction $y$ under the condition corresponding to monthly average of daily maximum temperature in January, Berbera (see Table 4a). Dimensions of the computational domain are 100 m and 20 m in the horizontal and vertical directions, respectively. The uniform square grid system was selected. The ground temperature was compared at 80 m downstream from the inlet.

evaporation rate at each moment in time to be predicted on the basis of wind speed, wind direction, and dry- and wet-bulb temperatures. Evaporation rate is then integrated over the year to get the total annual evaporation amount (per m² of evaporative pad) as a function of the greenhouse orientation (Fig. 12a). Table 6 shows the optimum angle for maximum evaporation, to maximise brine disposal rates for each location. As shown in Fig. 12(a), a rotation of wind direction through 180° leads to reverse air flow through the evaporator pads with the magnitude of flow maintained, resulting in the same evaporation rate
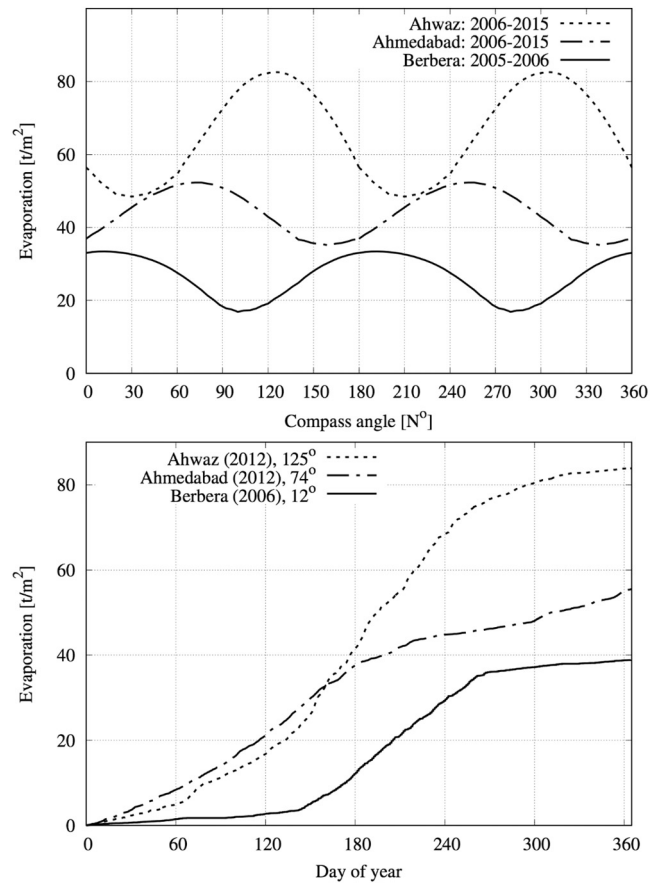


Fig. 12. Annual water evaporation in Berbera, Ahmedabad and Ahwaz, per m² of face area of evaporative cooling pad. (a) Effect of orientation (compass angle) of the system, and (b) cumulative evaporation over year.

**Table 6**
Results for evaporation rates and corresponding salt production outputs, for the optimal orientation as shown (data periods in Table 2), expressed per m² of face area of cooling pad.

| Location | Per m² of evaporative cooling pad face | | Optimal orientation [°N] |
|---|---|---|---|
| | Water evaporation [m³/m²·yr] | Salt production [tonne/m²·yr] | |
| Berbera | 33.4 | 2.34 | 12 |
| Ahwaz | 82.6 | 5.78 | 125 |
| Ahmedabad | 52.3 | 3.66 | 74 |

predicted (on the other hand, reversal of air flow would result in loss of satisfactory cooling performance because the cool wake would no longer be on the side of the evaporator pad where the shade net and crops are located). Fig. 12(b) shows how the water evaporation rate varies cumulatively throughout the year. The yearly evaporation rates vary among the case studies presented, from 33.4–82.6 m³ of water per face m² of evaporative cooling pad, with the greatest in Ahwaz and least in Berbera (Table 6). The high evaporation in Ahwaz is attributed to the typically low ambient humidity in this location.

As the water evaporates, it must be made up by replacing with an excess of brine, to prevent the salt concentration from becoming too high. A maximum concentration of 140 kg/m³ salt, corresponding to four times the concentration of normal seawater, has been assumed for the outlet brine discharged to the solar evaporation ponds (Fig. 1b). It is believed that this concentration may be handled by seawater evaporator pads without serious problems of salt encrustation (see Discussion). It is also noted that this concentration reduces the vapour

**Table 7**

Showing land areas needed to dispose of 1000 m$^3$/yr of brine at inlet concentration shown, with outlet brine at concentration of 140 kg/m$^3$ directed to evaporation pond in all cases. Use of the seawater greenhouse reduces the size of pond needed for brine disposal; and the total area needed for greenhouse + evaporator pond is less than when using an evaporation pond alone. (PET = Potential Evapotranspiration).

| Location | Concentration brine inlet | Evaporator pad area | Volume of water evaporated | Volume of concentrated brine remaining | Salt produced | PET | Evaporation pond size [m$^2$] | | Greenhouse area | Total area: greenhouse + evaporation pond |
|---|---|---|---|---|---|---|---|---|---|---|
| | kg/m$^3$ | m$^2$ | m$^3$/yr | m$^3$/yr | Tonnes/yr | m/yr | No greenhouse | With greenhouse | m$^2$ | m$^2$ |
| Berbera | 70 | 29.9 | 500 | 500 | 70 | 2 | 714 | 357 | 299 | 657 |
| Ahwaz | 70 | 19.1 | 500 | 500 | 70 | 1.6 | 893 | 446 | 191 | 638 |
| Ahmedabad | 35 | 12.1 | 750 | 250 | 35 | 2 | 714 | 179 | 121 | 300 |

pressure of the solution by < 10%, so evaporation rates are not expected to be affected unduly.

With these assumptions, Table 7 includes also details of the volume of the concentrated brine leaving the seawater greenhouse and the estimated land areas for the salt evaporation ponds in each case studied. The calculation is based on a brine volume of 1000 m$^3$/yr to be disposed of from the desalination plant (or other source); for smaller or greater volumes the results may be scaled accordingly.

For comparison with a more conventional brine disposal system, the corresponding area of salt evaporation ponds without prior volume reduction is also shown. This area is calculated based on local potential evapotranspiration multiplied by the factor 0.7, to account for lower evaporation from saline water as compared to freshwater, as suggested in [10]. Even if the area of the greenhouse cultivated land is included, the total area of the greenhouse + evaporation ponds is 40–90% that of the evaporation ponds alone: thus there is land saving in all cases. Further, at least half the hand utilised will be for purposes of growing crops thus adding value to the system. Total land requirements for disposal of 1000 m$^3$/yr of brine are in the range 300–657 m$^2$ (Table 7).

### 5.2. Airflow and climate inside greenhouse

This sub-section describes the modelling of the whole greenhouse, carried out with the help of the pressure drop coefficients determined for the evaporative cooling pad and the shade net, and using the Large Eddy Simulation turbulence model. At this stage, ground effects were no longer neglected, with the wall function and ground radiation model introduced. The predicted velocity vector fields, an example of which is
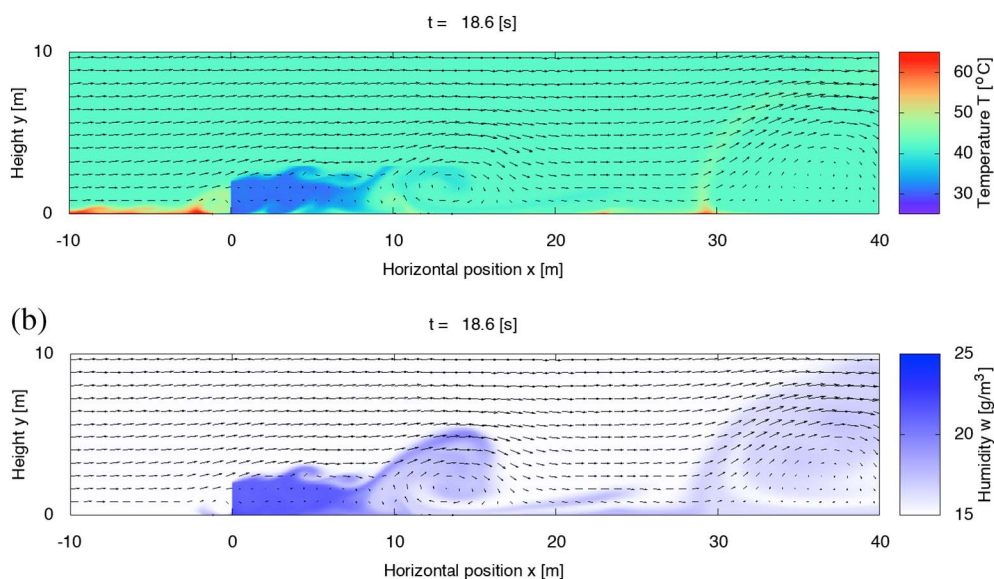
shown in Fig. 13, reveal a complex pattern of flow as the wind boundary layer impinging on the greenhouse structure. Disruption of the air flow as it passes over and through the evaporative cooling pad results in large vortices, which are not stationary, but shed resulting in breaking waves downstream. Shearing with the ground adds to this vorticity. The vortices are not precisely periodic but tend to occur with certain regularity at periods of around 1 s (refer to Movies A and B in Supplementary material). These unsteady vortices have a length scale comparable to the height of the structure. We note from the movies that a second, vertical plume tends to arise from the heated ground, downstream of the shade tent, veering to the right under the action of the wind.

The ground acts as a heat source and the mixing flow, together with the buoyancy of air heated by the ground, causes a gradual dissipation of the horizontal plume of cool air that emanates from the cooling pad. Mixing with the bulk airflow above the shade net also contributes to this dissipation (see Movies A and B).

Comparison of results among the three case studies gives insights the effect of the wind velocity on the length of the plume, as shown in Figs. 14–16 where time-averaged results (obtained by ensemble averaging with 1000 sample points at 1 s intervals) are provided to smooth out fluctuations due to the vortices. Ahwaz and Ahmedabad have relatively low wind velocities of 3.3 and 3.7 m/s respectively. In these cases the plume extends a little beyond 10 m. For the higher wind velocity in the Berbera case ($U_0$ = 10.7 m/s) the length of the cool plume is reduced slightly (Fig. 14). This is attributed to the lower effectiveness of the cooling pad due to the increased airflow velocity (as evident from Eq. (7)). A second reason is that the higher frequency disturbance in the



**Fig. 13.** Instantaneous (a) temperature and (b) humidity fields, corresponding to Berbera in July superimposed with velocity vectors (wind velocity $U_0$ = 10.7 m/s, evaporator pad height $H_{pad}$ = 1.5 m). The horizontal position x = 0 corresponds to the base of the front wall incorporating the evaporative cooling pad. Refer to Supplementary Movies A and B for corresponding animated versions.
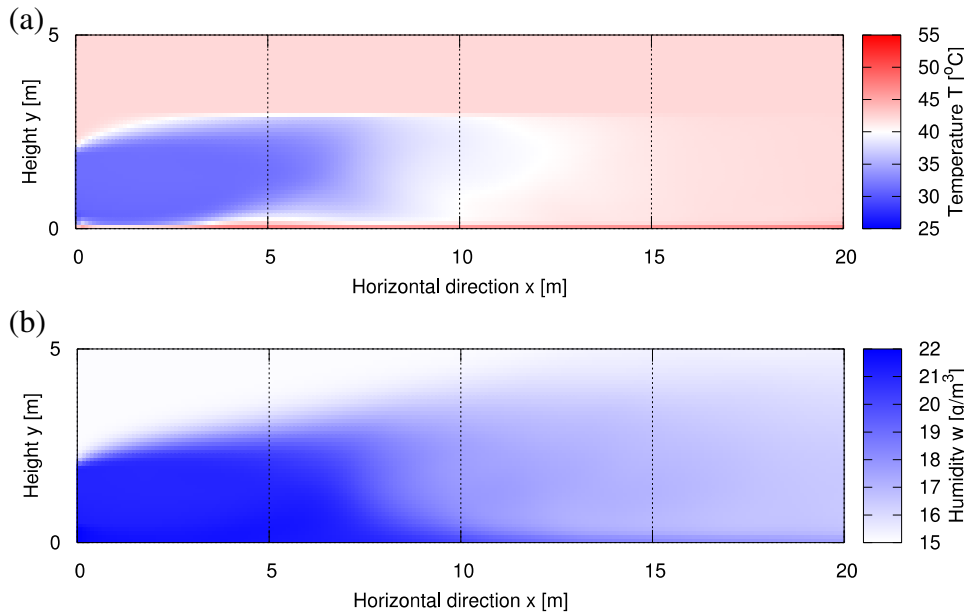
**Fig. 14.** Time-averaged temperature and humidity fields, according to horizontal and vertical coordinates measured from the base of the front wall of the greenhouse, Berbera, July. Pad height $H_{pad} = 1.5$ m, wind speed $U_0 = 10.7$ m/s, ambient temperature $T_{db} = 42.3$ °C, wet bulb temperature $T_{wb} = 25.8$ °C. Humidity at ambient and wet bulb conditions are 15.1 g/m$^3$ and 24.1 g/m$^3$ respectively. Solar radiation (shortwave) $G = 743$ W/m$^2$. Soil temperature $T_{soil} = 33.9$ °C at depth 0.1 m.

quasi-periodic plume enhances heat exchange with the ground below and bulk air flow above. This even suggests that it may be preferable to slow the air flow approaching the evaporative cooler (e.g. by means of additional nets to remove kinetic energy from the flow).

To assist in the choice of length of the greenhouse shade-net and cultivation area, Fig. 17 shows – for each of three locations – an average of temperature over a longitudinal section of the cultivation area. These plots confirm that the cooling effect starts to deteriorate at a position of $x = 10$ m and is mostly lost at $x = 15$ m.

The conditions chosen for Figs. 14–17 correspond to typical peak conditions temperature for the whole year, corresponding to one particular month in each location. To give a picture for the complete year, Fig. 18 shows how internal conditions for the shade net will vary month by month for the whole year. As noted above, around 10 m downstream of the evaporative pad, the cooling effect starts to dissipate and here we compare cases of temperature averaged over the first 10 m, or alternatively over the first 15 m, downstream. For the shorter length of 10 m, 8-10 °C of cooling is predicted in Berbera the hottest time of year

(June/July). In Ahwaz, where conditions are considerably drier, the cooling effect increases to 16 °C. In Ahmedabad, the climate follows a bimodal pattern due to the monsoon season. For the dry and hot month of May, we predict about 12 °C for this location. However, in November and December the prevailing wind reverses so that cooling would be on wrong side of the evaporative cooling pad – therefore result are not shown for this month.

If the longer length of 15 m is chosen for the calculation of average temperature, the corresponding results indicate 2–4 °C less cooling considering all locations.

### 5.3. Contribution of different components to cooling

In the proposed design, cooling results from the use of two components – the evaporative cooling pad and the shade net. Having modelled the combined cooling effect, it is now interesting to present results predicted using each of these components separately. Fig. 19 compares temperature as function of distance $x$ from the cooling pad
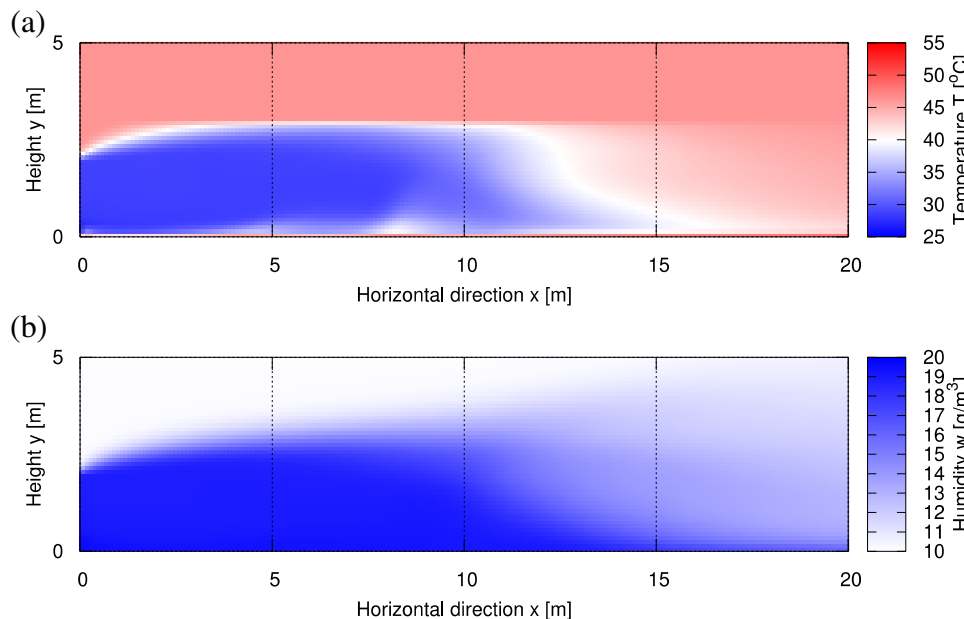


**Fig. 15.** Time-averaged temperature and humidity fields according to horizontal and vertical coordinates measured from the base of the front wall of the greenhouse, Ahwaz, August. Pad height $H_{pad} = 1.5$ m, wind speed $U_0 = 3.3$ m/s, ambient temperature $T_{db} = 46.3$ °C, wet bulb temperature $T_{wb} = 23.7$ °C. Humidity at ambient and wet bulb conditions are 10.1 g/m$^3$ and 21.4 g/m$^3$ respectively. Solar radiation (shortwave) $G = 778$ W/m$^2$. Soil temperature $T_{soil} = 34.1$ °C at depth 0.1 m.
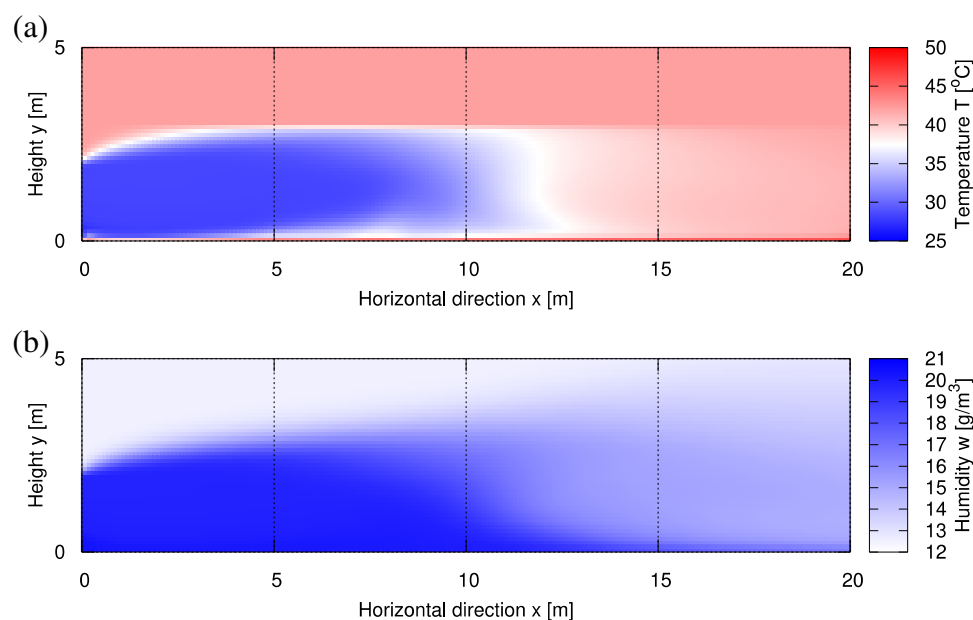
(a)



(b)



Fig. 16. Time-averaged temperature and humidity fields according to horizontal and vertical co-ordinates measured from the base of the front wall of the greenhouse, Ahmedabad, May. Pad height $H_{pad}$ = 1.5 m, wind speed $U_0$ = 3.7 m/s, ambient temperature $T_{db}$ = 42.1 °C, wet bulb temperature $T_{wb}$ = 24.2 °C. Humidity at ambient and wet bulb conditions are 12.5 g/m$^3$ and 22.0 g/m$^3$ respectively. Solar radiation (shortwave) $G$ = 800 W/m$^2$. Soil temperature $T_{soil}$ = 30.6 °C at depth 0.1 m.

with and without the use of a shading net, showing that removing the shade net but keeping the evaporative cooling pad has an important effect on cooling: the length of the cool region is halved to about 5–7.5 m compared to that achieved with both components. This is because the shade net, besides reducing the solar radiation input, helps to contain the cool air from the evaporative cooling pad, slowing mixing with the ambient air at dry bulb temperature. Use of the shading net alone is not effective in cooling, with temperatures rising above the dry bulb temperature (Fig. 19). Nonetheless, the shade net alone would be useful to reduce solar radiation on the foliage, increasing local humidity and lowering water requirements, among other benefits [23,61].

## 6. Discussion

In this paper we have presented a novel approach to brine disposal whereby the brine is valorised for cooling of a shade-net type greenhouse (Seawater Greenhouse). The comparison to open-pond evaporation is generally favourable, in terms of land usage, presenting an 8–58% reduction in land footprint compared to conventional open ponds (Table 7). Though this is less saving than achieved with the WAIV system [13] – which gave as much as an order of magnitude reduction in land footprint – the benefit of the current system is that it gives added value to the land used in the evaporation system, by providing a protected area for cultivation.

This estimate of land usage reduction is for a greenhouse that is 15 m long in the direction the air flow (i.e. perpendicular to the cooling pads). For longer lengths the land usage estimate will be increased, but the length of 15 m was chosen on the basis of the cooling computations which showed that beyond this length the cooling effect dissipates with the internal temperature returning to the ambient temperature. In fact, even with 15 m length the real land usage may be greater than in Table 7, to prevent too much influence of one cooling pad on the next one that may be positioned downwind. So, closer spacing among evaporative cooling walls will be favourable to maximise cooling, while more distant spacing will favour evaporation rate per m$^2$ of evaporative cooling pad. Ultimately, the optimum spacing will depend on site specific constraints and economic considerations.

Though a full economic study would call for proper analysis based on local markets, some preliminary comments can be made as regards land revenue for a given land footprint of brine disposal systems. An illustrative example shown in Table 8 below compares revenue from 1 ha of land utilised by a seawater greenhouse installation (including

evaporation pond and greenhouse, thus yielding both salt and tomato crop) against revenue from the same land area for production of just salt in conventional evaporation ponds. In both cases, the system is receiving desalination brine and the example is based on the findings from the Berbera case study.

With the nominal assumptions shown, it is interesting to note that nearly 3 times revenue increase is estimated, due primarily to the additional revenue from tomato production, exceeding somewhat the revenue from salt production which only increases marginally. It is interesting to point out, however, that since both revenue streams are potentially significant it would be important to have access to markets for both salt and tomato produce for the most effective business model.

The cooling and wind-protection effects of this system can be compared against a standard pad-and-fan greenhouse with impermeable polythene cladding. In the pad-and-fan greenhouse, a temperature gradient occurs from the air entrance at the pad, to the air exit near the fan. Kittas et al. [66] reported an 8 °C temperature rise over a 60 m long greenhouse containing a rose crop. Watt and Brown recommend 30.5 to 68.8 m (100–225 ft) length to minimise pad-to-fan temperature differences [67]. In this study, a comparable temperature rise is predicted over a considerably shorter length of only 10–15 m. This is a substantial shortening of cooled area, not readily explained by the absence of crop, and attributed mainly to the mixing of hot air from outside the shade net (Fig. 13). Using the shade-net arrangement, the cooled area will be less for a given amount of evaporative cooling pad such that more cooling pad may be needed for given cultivated area. On the other hand, the shade net construction can be considered favourable from the point of view of minimising the cost of the cladding and support structure – and from the point of view of durability of the cladding. Polythene degrades under sunlight, requiring replacement every 2–3 years. This introduces expense but also the difficulty of disposal of the cladding. Furthermore, the possible closer spacing of evaporative cooling pads in the proposed shade-net arrangement can be considered favourable from the point of view of maximising brine disposal.

A greenhouse that relies on wind ventilation, as proposed here, has to be specified carefully with respect to local wind conditions. A site with consistently still wind conditions would not be suitable. We have identified that a wind speed of 3 m/s is sufficient for satisfactory cooling (though higher wind speeds will increase salt production). Changes in wind direction will be problematic. This can be addressed to some extent by a double evaporative cooling wall structure to shelter the crops on two sides – to accept a reversal of wind direction. Since in
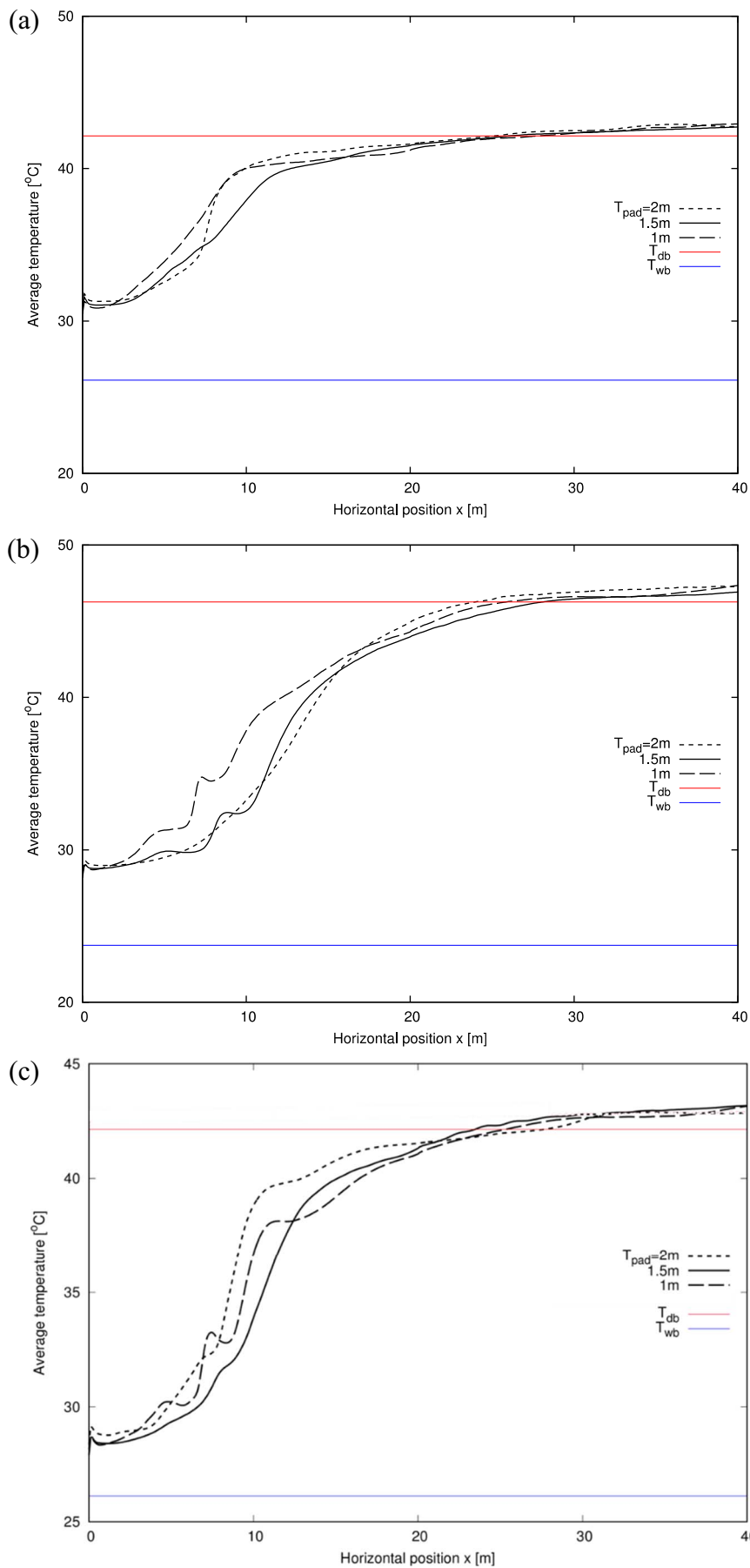
**Fig. 17.** (a) Average temperature (*T*) as a function of distance downstream from evaporative cooling pad (*x*). The temperature is averaged between ground surface and a height corresponding to the top of the cooling pad, and also time averaged. The results are shown for three different heights of cooling pad (1, 1.5 and 2 m) and for the locations of (a) Berbera (b) Ahwaz and (c) Ahmedabad – for conditions see legends to Figs. 14–16.
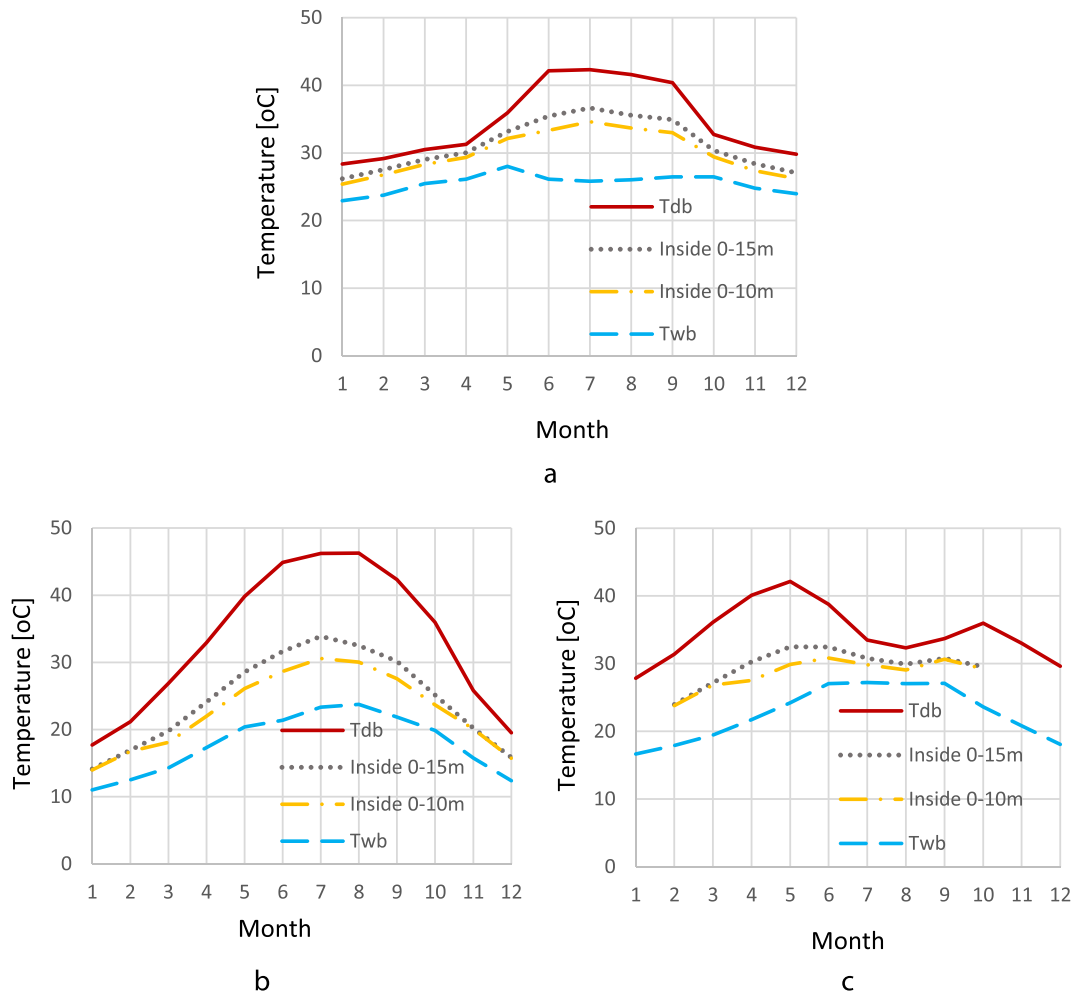
**Fig. 18.** Comparison of the temperature inside and outside the shade house for a typical day of each month based on average daily maximum temperature over the month. The graphs compared ambient dry bulb temperature $T_{db}$ and ambient with wet bulb temperature $T_{wb}$, with a temporal-spatial average of temperature over an area extending vertically to the top of the cooling pad and horizontally either 10 m or 15 m (chain-dotted line and dotted line respectively). Three cases: (a) Berbera, Somaliland (b) Ahwaz, Iran and (c) Ahmedabad, India.
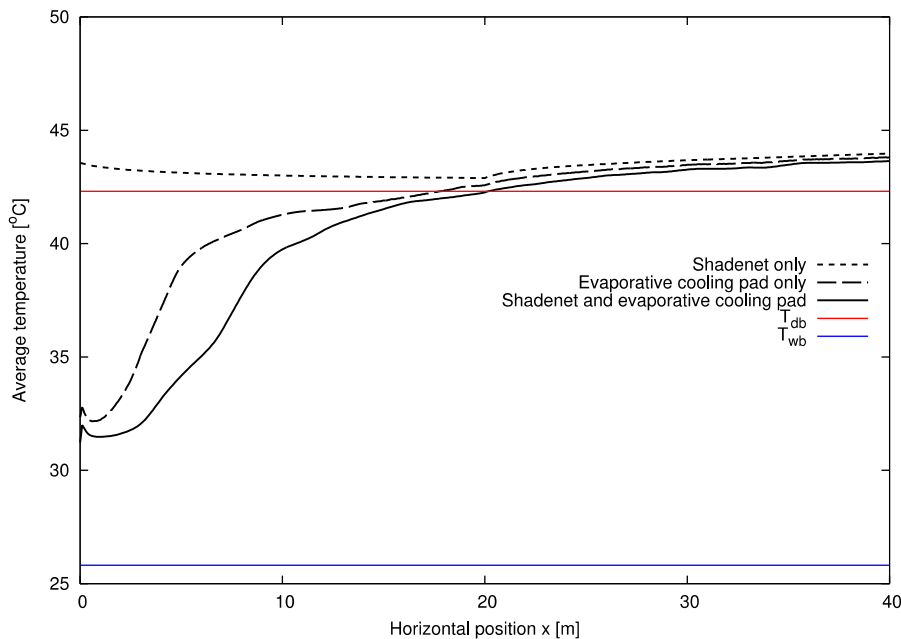


**Fig. 19.** Cooling effect using the evaporative cooling pad only and shade net only (Berbera) compared to using both components (as in Fig. 17a).

**Table 8**
Preliminary economic comparison of revenue from brine disposal options each occupying 1 ha of land: the proposed seawater greenhouse installation is compared to a conventional evaporation pond to show an estimated increase in revenue per land footprint (Berbera).

|  | Unit | Seawater greenhouse installation | Conventional evaporation ponds |
|---|---|---|---|
| Evap. pond area | Hectare | 0.46 | 1 |
| Greenhouse area | Hectare | 0.54 | 0 |
| Salt production | Tonnes/yr | 1070 | 980 |
| Tomato yield @ 30 kg/m$^2$/yr[a] | Tonnes/yr | 163 | 0 |
| Salt Value @$100/ tonne[b] | $1000 | 107 | 98 |
| Crop value @$1000/ tonne | $1000 | 163 | 0 |
| Irrigation cost @$1/ m$^3$ [c] | $1000 | − 8 | 0 |
| Total revenue | $1000 | 262 | 98 |

[a] Estimated yield, below that for modern cultivation systems achieving > 50 kg/m$^2$ yr [62], since the system is intended for use in locations with relatively limited technical support.

[b] Intermediate estimate with respect to lower figure of $40–$50/tonne and higher estimate of $150/tonne [63].

[c] Based on desalinated water cost of $1/m$^3$ and water use efficiency of 20 kg/m$^3$ [64,65].

large projects, evaporative cooling walls are likely to be laid out at periodic intervals, this need not add to expense significantly. It can also be mentioned that, unlike in a 'polytunnel' greenhouse, temporary failure of the cooling system would not generally result in catastrophic overheating due to the porous nature of the cladding.

In assessing the use of seawater greenhouses for brine valorisation, this paper has focussed on the modelling and conceptual design aspects. For reliable operation, however, a number of practical aspects will also need to be addressed. For example, management of low-solubility calcium salts will be important to avoid blockage or uneven flow in the evaporative cooling pads. Preliminary calculations using the Smith and Davis Stability Index (S & DSI) indicate that, for conditions prevalent in the North Indian Ocean [68], a threshold pH of about 8 applies above which precipitation occurs. As the seawater becomes more concentrated, giving increased concentration of calcium and alkalinity, the S & DSI will lower to about 6.8 suggesting a risk of calcium carbonate precipitation in the cooling pads. Nonetheless, earlier Seawater Greenhouses have been operated [69] leading to the practical observation that precipitation tends to occur mainly in the sump tanks of the evaporative cooling pads, rather than on the pads themselves. This may be attributable to the relatively stagnant conditions within the tanks relative to the continuously flowing conditions in the evaporator pads, as indeed the S & DSI prediction applies to equilibrium conditions and certain time lag in the precipitation of scaling species can be expected.

Another consideration is $CO_2$ stripping in the evaporator pads. This may further raise pH and aggravate scaling. On the other hand, $CO_2$ stripping by bubbling has recently been investigated as a tool to reduce $CO_2$ levels in coastal marine ecosystems [70]. It has been pointed out that pH variation in coastal ecosystems is much more marked than in open oceans, due to anthropogenic and other influences, and can actually result in substantially lower pH values than in the open ocean [71]. This suggests that the assessment of scaling has to be done in relation to local sea conditions. Strategies to manage scaling include: (i) acid dosing at the RO inlet with HCl (proprietary anti-scalants are not preferred to avoiding contaminant the salt which may be destined for food use) and (ii) periodic flushing of evaporator pads and sump tanks with raw seawater which is any case desirable to remove accumulation of sand and dust carried by the wind.

For future work, we envisage several areas. Firstly, it will be important to complete validation of the modelling through comparisons to a fully functioning system to be implemented at one of the case study locations. Implementation will also be important for understanding and overcoming practical challenges such as avoiding salt build up on the pads, as discussed above, and managing any salt spray. Secondly, we envisage a number of future improvements to the modelling process. Input data quality is at present limited in many locations of interest, particularly as regards frequency of measurements and accuracy of solar radiation data. The Baseline Surface Radiation Network provides measurements at intervals of less than 1-hour for several stations around the world and is currently being extended [72]. Greater use of remote sensed data will also be of interest to provide global coverage. As regards the model algorithms, we wish to extend the model for 3D effects, including end effects from the structure, and for cases where there are repeated structures of seawater greenhouses over large area installations. Repeated placement of evaporative cooling walls would also help maintain cooling under reversed wind conditions, with crops planted on either side of each wall.

Another aspect will the incorporation of crop models. For example, Bartanzas et al. have modelled greenhouse crops using a porous medium approach, quite similar to that used here for the evaporative pads and the shade net [73,74]. Together with inclusion of evapotranspiration models, and more accurate data for moisture exchange at ground level, this could be expected to result in predictions of improved cooling performance, depending on the choice of crop, stage of growth, and method of irrigation.

A further simplifying aspect of the current modelling is the use of a constant 'velocity reduction factor' to predict approximate evaporation rates per pad area, independently of evaporator height, construction details, and approaching boundary layer profile dependent on ground terrain. A more sophisticated approach may allow in future for more detailed design parameters to be explored with regard to component dimensions and detailed wind conditions that may become available for particular sites.

Finally, because of the sensitivity to local conditions and the increasing interest in the technology, it will be important to incorporate the model into a Decision Support Tool for site selection and design purposes. The tool should be user-friendly and fast in execution, so that it can be taken up by a range of users wishing to explore quickly numerous design cases of interest.

## 7. Conclusions

This paper has presented modelling and predictions for a brine valorisation method using evaporative cooling of seawater greenhouses with wind-driven air flow. The model has been validated with the help of satellite-measurements of ground temperature. The main conclusions of the modelling are:

1. A velocity reduction factor of 0.31 characterises the evaporative cooling pad, independent of the location and climatic conditions, such that the brine reduction rate is proportional to the face area of evaporative cooling pad used. According to location, evaporation rates per face area have been predicted in the range 33 to 83 m$^3$/ m$^2$ yr.

2. Solar evaporation ponds are still needed for 'zero liquid discharge', but with lesser pond area due to the volume reduction of the brine by evaporation. Taking into account total land usage for greenhouses and evaporation ponds, a reduction in total land footprint of 8–58% is predicted.

3. The evaporative cooling pad provides a horizontal plume of cold air that is useful for space cooling of the crop cultivation area. The plume persists substantially for about 10 m downstream of the evaporative cooling pad, reducing peak season temperatures by 8–16 °C (depending on location). Correspondingly, air moisture content is increased by 6–9 g/m$^3$ over this 10 m length. At 15 m

downstream the plume is mostly dissipated.

4. Investigation of the effects of individual components has shown that, while the shade-net does not alone provide effective cooling, it helps to contain the cold air plume from the evaporative cooling pad. Without the shade net, the useful length of the plume is roughly halved.

5. A greater wind speed does not necessarily provide a longer plume for cooling, due to lowered effectiveness of the evaporative cooling pad and due to more vigorous mixing with hot air near the ground and with the surrounding air stream.

6. Since the validation against satellite data shows that the model may overpredict ground temperature, it is estimated that temperature in the cropping area of the greenhouse may be in error by 0 to $+5\,°C$ i.e. real temperatures are expected to be lower than the predicted ones. Temperature will be lowered further once crops are included, as the model predictions are for dry ground.

It is concluded that the design has significant potential as a novel approach to brine disposal. It adds value to the brine by facilitating crop cultivation and salt production. As a zero liquid discharge system, it has generally lower land footprint than conventional evaporation ponds.

Supplementary data to this article can be found online at https://doi.org/10.1016/j.desal.2017.10.025.

## Nomenclature

| Variable | Physical quantity | (Unit) |
|---|---|---|
| A | Pad orientation in compass angle | (N°) |
| AM | Air mass | (−) |
| C | Quadratic pressure drop coefficient | (−) |
| c | Phase velocity | (m/s) |
| CC | Cloud cover ranged between 0 and 1 | (−) |
| $c_p$ | Specific heat capacity at constant pressure for air | (J/kg/K) |
| d | Hole diameter of shade net | (m) |
| $D_w$ | Diffusion coefficient for water vapour in air | (m²/s) |
| g | Absolute value of the gravity acceleration on the earth: 9.8 | (m/s²) |
| $H_{air}$ | Thickness of air layer | (m) |
| $H_{pad}$ | Pad height | (m) |
| $H_{soil}$ | Thickness of soil layer | (m) |
| $H_w$ | Wall height ( = pad elevation) | (m) |
| $L_{pad}$ | Length of computational domain | (m) |
| $\Delta P$ | Pressure difference | (Pa) |
| P | Pressure | (Pa) |
| R | Horizontal short wave solar radiation | (W/m²) |
| $R_d$ | Intensity of short wave solar radiation | (W/m²) |
| t | Time | (s) |
| $T_{db}$ | Dry bulb temperature ( = Ambient temperature) | (K, °C) |
| $T_{db}\uparrow$ | Monthly average of the daily maximum of dry bulb temperature | (K, °C) |
| $T_{db}\downarrow$ | Monthly average of the daily minimum of dry bulb temperature | (K, °C) |
| $T_{pad}$ | Pad temperature | (K, °C) |
| $t_{pad}$ | Pad thickness | (m) |
| $T_{soil}$ | Soil temperature | (K, °C) |
| $T_{sky}$ | Sky temperature | (K, °C) |
| $T_{wb}$ | Wet bulb temperature | (K, °C) |
| $T_{wb}\uparrow$ | Monthly average of the daily maximum of wet bulb temperature | (K, °C) |
| $T_{wb}\downarrow$ | Monthly average of the daily minimum of wet bulb temperature | (K, °C) |
| $U_0$ | Ambient wind speed | (m/s) |
| $U_{ref}$ | Reference wind speed defined at the reference height $Y_{ref}$ | (m/s) |
| **u** | Velocity vector | (m/s) |
| u, v, $u_z$ | Components of velocity vector $u$ in the $x, y, z$ coordinates | (m/s) |
| w | Water vapour content in air (absolute humidity) | (kg/m³) |
| **x** | Position vector | (m) |
| x, y, z | Cartesian coordinates | (m) |
| $Y_{ref}$ | Reference height defined with the reference wind speed $U_{ref}$ | (m) |

*Greek symbols*

| Variable | Physical quantity | (Unit) |
|---|---|---|
| β | Thermal expansion ratio of air | (−) |
| γ | air exclusion ratio by water vapour | (m³/kg) |
| η | Saturated efficiency of cardboard | (−) |
| φ | Porosity of shade net | (−) |
| κ | Thermal diffusivity of air | (m²/s) |
| $\lambda_{air}$ | Thermal conductivity for air layer | (W/m·K) |
| $\lambda_{soil}$ | Thermal conductivity for soil | (W/m·K) |
| μ | Viscosity of air | (Pa·s) |
| ρ | Density | (kg/m³) |
| $\rho_{air}$ | Density of air | (kg/m³) |
| σ | Stefan-Boltzmann constant ($5.67 \times 10^{-8}$) | (W/m²/K⁴) |
| χ | Pressure drop coefficient per unit length | (m⁻¹) |
| $\xi_{pad}$ | Quadratic wind resistance factor of evaporator | (−) |
| $\xi_{net}$ | Quadratic wind resistance factor of shade net | (−) |
| ζ | Zenith angle | (rad) |

## Appendix A. Properties of evaporative cooling pad

Fig. A below shows the agreement between manufacturers' data [39] and the correlations used in this study. Fig. A(a) uses the pressure drop coefficient of C = 14.4 and Fig. A(b) uses Eq. (7) (Section 4.1).
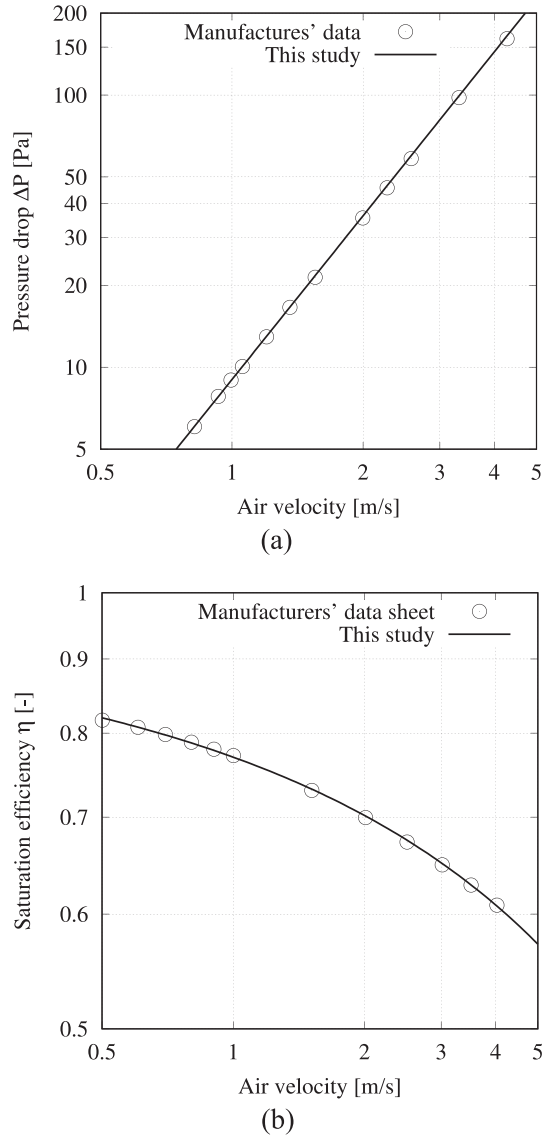
(a)



(b)

Fig. A. Correlations for (a) wind resistance and (b) saturation efficiency as a function of air velocity are depicted together with comparison with manufacturers' data (pad thickness 0.1 m).

## Appendix B. Psychrometric relations

The absolute humidity $w$ [kg/m$^3$] at saturation is determined from the gas equation as:

$$w = \frac{M_{H_2O}\, P_{H_2O}}{R_0\, T_{abs}},$$

(B.1)

where the molar mass of water $M_{H_2O} = 18.015$ [kg/kmol], $P_{H_2O}$ [Pa] is the vapour pressure of the water, and $T_{abs}$ is the absolute temperature [K], respectively, and $R_0$ is the gas constant ($= 8314.5$ J/kg K). The vapour pressure of water is approximated by Wexler-Hyland equation [75] as a function of temperature only in the range $T_{abs} = 273$ to 473 K:

$$ln\, P_{H_2O} = -\frac{5.8002206 \times 10^3}{T_{abs}} + 1.3914993 - 4.8640239 \times 10^{-2}\, T_{abs} + 4.1764768 \times 10^{-5}\, (T_{abs})^2 - 1.4452093 \times 10^{-8}(T_{abs})^3 + 6.5459673\, \log(T_{abs}).$$

(B.2)

Weather data are supplied in terms of dry-bulb temperature and dew point $T_{dew}$. The above equations are thus used to determine $w$ correspondingly with $T_{abs} = T_{dew}$, which is then used to determine the relative humidity as $w/w_{sat}$ where $w_{sat}$ is calculated from the above equations with $T_{abs} = T_{dry}$. To convert this information to wet-bulb temperature, the following relation is used [76]:

$$T_{wb} = T_{db}tan^{-1}\left[0.151977(RH + 8.313659)^{\frac{1}{2}}\right] + tan^{-1}(T_{db} + RH) - tan^{-1}(RH - 1.676331) + 0.00391838(RH)^{\frac{3}{2}}tan^{-1}(0.023101RH) - 4.686035.$$

(B.3)

Finally, the wet-bulb humidity $w_{wet}$ it calculated by substituting $T_{wet}$ in Eq. B.2.

# References

[1] D.H. Kim, A review of desalting process techniques and economic analysis of the recovery of salts from retentates, Desalination 270 (1) (2011) 1–8.

[2] A. Pérez-González, et al., State of the art and review on the treatment technologies of water reverse osmosis concentrates, Water Res. 46 (2) (2012) 267–283.

[3] A. Shahmansouri, et al., Feasibility of extracting valuable minerals from desalination concentrate: a comprehensive literature review, J. Clean. Prod. 100 (2015) 4–16.

[4] J. Liu, et al., Concentrating brine from seawater desalination process by nanofiltration–electrodialysis integrated membrane technology, Desalination 390 (2016) 53–61.

[5] The Salt Institute, Available from: http://www.saltinstitute.org/ , Accessed date: 15 January 2017.

[6] S. Al-Sanea, J. Orfi, A. Najib, Numerical study of flow, temperature, and salinity distributions of a brine discharge problem, Desalin. Water Treat. 55 (12) (2015) 3218–3230.

[7] L.J. Falkenberg, C.A. Styan, The use of simulated whole effluents in toxicity assessments: a review of case studies from reverse osmosis desalination plants, Desalination 368 (2015) 3–9.

[8] L. Katzir, Y. Volkmann, N. Daltrophe, E. Korngold, R. Mesalem, Y. Oren, J. Gilron, WAIV-Wind aided intensified evaporation for brine volume reduction and generating mineral byproducts, Desalin. Water Treat. 13 (1–3) (2010) 63–73.

[9] A. Ravizky, N. Nadav, Salt production by the evaporation of SWRO brine in Eilat: a success story, Desalination 205 (1) (2007) 374–379.

[10] M. Ahmed, et al., Use of evaporation ponds for brine disposal in desalination plants, Desalination 130 (2) (2000) 155–168.

[11] F.A. Rodríguez, D.E. Santiago, N.F. Suárez, J.O. Méndez, J.M. Veza, Comparison of evaporation rates for seawater and brine from reverse osmosis in traditional salt works: empirical correlations, Water Sci. Technol. Water Supply 12 (2) (2012) 234–240.

[12] J.-P. Nicot, et al., Self-Sealing Evaporation Ponds for Desalination Facilities in Texas, Texas Water Development Board, 2007.

[13] F. Macedonio, et al., Wind-Aided Intensified eVaporation (WAIV) and Membrane Crystallizer (MCr) integrated brackish water desalination process: advantages and drawbacks, Desalination 273 (1) (2011) 127–135.

[14] M. Turek, P. Dydo, R. Klimek, Salt production from coal-mine brine in ED–evaporation–crystallization system, Desalination 184 (1) (2005) 439–446.

[15] C. Fernández-González, et al., Electrodialysis with bipolar membranes for valorization of brines, Sep. Purif. Rev. 45 (4) (2016) 275–287.

[16] Y. Tanaka, et al., Ion-exchange membrane electrodialytic salt production using brine discharged from a reverse osmosis seawater desalination plant, J. Membr. Sci. 222 (1–2) (2003) 71–86.

[17] Iodine Global Network, http://www.ign.org , Accessed date: 20 January 2017.

[18] M. Andersson, B. de Benoist, L. Rogers, Epidemiology of iodine deficiency: salt iodisation and iodine status, Best Pract. Res. Clin. Endocrinol. Metab. 24 (1) (2010) 1–11.

[19] C. Paton, P. Davies, The seawater greenhouse for arid lands, Mediterranean Conference on Renewable Energy Sources for water Production. Santorini, Greece, 1996.

[20] A. Klein, First Farm to Grow Veg in a Desert Using Only Sun and Seawater, New Scientist, (6 Oct 2016).

[21] C. Paton, Vapour Value, Global Water Forum, (1 April 2014).

[22] M. Möller, S. Assouline, Effects of a shading screen on microclimate and crop water requirements, Irrig. Sci. 25 (2007) 171–181.

[23] J. Tanny, U. Dicken, S. Cohen, Vertical variation in turbulence statistics and energy balance in a banana screenhouse, Biosyst. Eng. 106 (2010) 175–187.

[24] NOAA, National climate center data, https://www7.ncdc.noaa.gov/CDO/cdo , Accessed date: 20 December 2016.

[25] Klimatafel von Berbera/Somalia. Baseline climate means (1961–1990) from stations all over the world (in German). Deutscher Wetterdienst. [retrieved 22 October 2016].

[26] Monthly Total Precipitation in Ahwaz by Month 1951–2010. Iran Meteorological Organization [retrieved 8 April 2015].

[27] Ahmedabad Climatological Table Period: 1981–2010. India Meteorological Department. [retrieved 25 March 2015].

[28] Michael Aliprandini, Our World, (January, 2016).

[29] https://agritech.blog.gov.uk/2015/06/18/seawatergreenhouse/ , Accessed date: 17 December 2017.

[30] Global Iodine Nutrition Scorecard, Available from: http://www.ign.org/cm_data/Scorecard_2015_August_26_new.pdf , .

[31] D. Mahjoob Farshchi, et al., Upper Gotvand Dam and hydro power plant: dealing with salinity in reservoir, challenges, remedies and evaluations, Int. Symp. Dams Global Environmental Challenges, 2014.

[32] Salt Commissioner, Ministry of Commerce and Industry, Govt of India, http://saltcomindia.gov.in/industry_india.html?tp=Salt , Accessed date: 20 January 2017.

[33] P.B. Andharia, Salt pan workers in Gujarat: examining the need for a special legislation, Available at SSRN, 2011. https://ssrn.com/abstract=1922287, .

[34] Alkali Manufacturers of India, http://ama-india.org/member-companies/ , Accessed date: 20 January 2017.

[35] Gujarat Infrastructure Development Board, Water supply scenario in Gujarat, http://www.gidb.org/water-supply-scenario-in-gujarat , Accessed date: 20 January 2017.

[36] J.H. Rah, et al., Towards universal salt iodisation in India: achievements, challenges and future actions, Matern. Child Nutr. 11 (4) (2015) 483–496.

[37] K. Yadav, et al., Successful implementation of a laboratory iodization quality assurance system in small-scale salt production facilities in India, Public Health Nutr. 17 (12) (2014) 2816–2823.

[38] J.R. Welty, C.E. Wicks, R.E. Wilson, Fundamentals of Momentum, Heat, and Mass Transfer, 5th edition, John Wiley & Sons, New York, 2008 (Table J.1).

[39] Munters CELdek®, 7090-15 evaporative cooling pad, product data sheet, https://www.munters.com/globalassets/inriver/resources/products/coolers-humidifiers/1782-celdek-7090_15_gb.pdf , Accessed date: 6 August 2017.

[40] J. Smagorinsky, General circulation experiments with the primitive equations, Mon. Weather Rev. 91 (3) (1963) 99–164.

[41] J. Deardorff, A numerical study of three-dimensional turbulent channel flow at large Reynolds numbers, J. Fluid Mech. 41 (2) (1970) 453–480.

[42] U. Ghia, et al., High-Re solutions for incompressible flow using the Navier-Stokes equations and a multigrid method, J. Comput. Phys. 48 (3) (1982) 387–411.

[43] J. Kim, P. Moin, J. Comput. Phys. 59 (1985) 308323.

[44] T. Kawamura, K. Kuwahara, Computation of High Reynolds Number Flow Around a Circular Cylinder With Surface Roughness, AIAA-84-0340, (1984), pp. 9–12.

[45] New Energy and Industrial Technology Development Organization, Guide Book for Installation of Wind Power Generator (in Japanese), NEDO, Japan, 2008, p. 76 http://www.nedo.go.jp/content/100797380ok.pdf , v.9.

[46] D.B. Spalding, A single formula for the law of the wall, J. Appl. Mech. E 28 (1961) 455–458.

[47] H. Schlichting, K. Gersten, Boundary-Layer Theory, 8th revised ed., (2000), pp. 522–524.

[48] Nikuradse, Stromungsgesetze in Rauhen Rohren., V. D. I. Forshungsheft No 361, 1933. (or Translation of "Stromungsgesetze in Rauhen Rohren." NACA, Technical memorandum (TM) 1929, Washington), (1950).

[49] B.M. Sorensen, Renewable Energy, Elsevier, 4th edition, (2010).

[50] M. Cekon, Accuracy analysis of longwave sky radiation models in the MZELWE module of the ESP-r program, Energ. Buildings 103 (2015) 147–158.

[51] J.A. Clarke, Energy Simulation in Building Design, 2nd edition, Butterworth-Heinemann, Oxford, 2001, p. 362.

[52] M. Janecek, Reflectivity spectra for commonly used reflectors, IEEE Trans. Nucl. Sci. 59 (3) (2012) 490–497.

[53] W.F. Ruddiman, Earth's Climate, Past and Future, Chapter 2, Freeman, 2001.

[54] International Organization for Standardization, Standard Atmosphere, ISO 2533:1975, (1975).

[55] M. Kamichika, et al., Micrometeorological Characteristics in a Sand Dune (I) on the Heat Balance Properties, 20 Bull. Sand Dune Res. Inst., Tottori Univ, 1981, pp. 1–9.

[56] M. Kitahara, et al., Effect of pavement on sultry night in urban town, The 46th Annual Meeting of the Japan Society of Civil Engineers, 2001, pp. 254–255.

[57] S. Jovic, D.M. Driver, Backward-facing Step Measurements at Low Reynolds Number, Reh = 5000, NASA Technical Memorandum 108807, (1994).

[58] I.E. Idelchik, Handbook of Hydraulic Resistance, Springer, 1996.

[59] M. Teitel, D. Dvorkin, Y. Haim, J. Tanny, I. Seginer, Comparison of measured and simulated flow through screens: effects of screen inclination and porosity, Biosyst. Eng. 104 (2009) 404–416.

[60] B.Y. Guo, Q.F. Hou, A.B. Yu, L.F. Li, J. Guo, Numerical modelling of the gas flow through perforated plates, Chem. Eng. Res. Des. 9 (1) (2013) 403–440.

[61] J. Tanny, S. Cohen, Y. Israeli, Screen constructions: microclimate and water use in Israel, XXVIII International Horticultural Congress on Science and Horticulture for People (IHC2010): International Symposium on 927, 2010.

[62] M.M. Peet, G.W.H. Welles, Greenhouse tomato production, Crop Production Science in Horticulture, 13 2005, p. 257.

[63] Salt Sellers, The Economist, http://www.economist.com/node/15276675, (Jan 14, 2010).

[64] N. Voutchkov, Desalination – Past, Present and Future, IWA, 2016, http://www.iwa-network.org/desalination-past-present-future/ , Accessed date: 6 February 2017.

[65] L. Zotarelli, J.M. Scholberg, M.D. Dukes, R. Muñoz-Carpena, J. Icerman, Tomato yield, biomass accumulation, root distribution and irrigation water use efficiency on a sandy soil, as affected by nitrogen rate and irrigation scheduling, Agric. Water Manag. 96 (1) (January 2009) 23–34 (ISSN 0378-3774).

[66] C. Kittas, T. Bartzanas, A. Jaffrin, Temperature gradients in a partially shaded large greenhouse equipped with evaporative cooling pads, Biosyst. Eng. 85 (1) (2003) 87–94.

[67] J.R. Watt, W.K. Brown, Evaporative Air Conditioning Handbook, Fairmont Press, Third edition, 1997.

[68] T. Takahashi, W.S. Broecker, A.E. Bainbridge, The alkalinity and total carbon dioxide concentration in the world oceans, Carbon Cycle Modelling, SCOPE 16.3078, 1981, pp. 271–286.

[69] P.A. Davies, K. Turner, C. Paton, Potential of the Seawater Greenhouse in Middle Eastern climates, International Engineering Conference Mutah 2004, Mutah, Jordan, (2004), pp. 523–540.

[70] D.A. Koweek, et al., Bubble stripping as a tool to reduce high dissolved $CO_2$ in coastal marine ecosystems, Environ. Sci. Technol. 50 (2016) 3790–3797.

[71] C.M. Duarte, I.E. Hendriks, T.S. Moore, Y.S. Olsen, A. Steckbauer, L. Ramajo, J. Carstensen, J.A. Trotter, M. McCulloch, Is ocean acidification an open-ocean syndrome? Understanding anthropogenic impacts on seawater pH, Estuar. Coasts 36 (2013) 221–236.

[72] World Radiation Monitoring Center-Baseline Surface Radiation Network, http://bsrn.awi.de , Accessed date: 6 December 2017.

[73] T. Bartznas, T. Boulard, C. Kittas, Numerical simulation of the airflow and temperature distribution in a tunnel greenhouse equipped with insect-proof screen in the opening, Comput. Electron. Agric. 34 (2002) 207–221.

[74] T. Bartzanas, T. Boulard, C. Kittas, Effect of vent arrangement on windward ventilation of a tunnel greenhouse, Biosyst. Eng. 88 (4) (2004) 479–490.

[75] R.W. Hyland, A. Wexler, Formulations for the thermodynamic properties of the saturated phases of $H_2O$ from 173.15 K to 473.15 K, ASHRAE Trans. 89 (2A) (1983) 500–519.

[76] R. Stull, Wet-bulb temperature from relative humidity and air temperature, Am. Meteorol. Soc. (2011) 2267–2269, http://dx.doi.org/10.1175/JAMC-D-11-0143.1.